Supporting Information
Turning on and off photoinduced electron transfer in fluorescent proteins by π-stacking, halide binding, and Tyr145 mutations

Alexey M. Bogdanov[a,b,#], Atanu Acharya[c,#], Anastasia V. Titelmayer[a],
Anastasia V. Mamontova[a], Ksenia B. Bravaya[d], Anatoly B. Kolomeisky[e],
Konstantin A. Lukyanov[a,b], Anna I. Krylov[c]

[a] Shemiakin-Ovchinnikov Institute of Bioorganic Chemistry, Moscow, Russia
[b] Nizhny Novgorod State Medical Academy, Nizhny Novgorod, Russia
[c] Department of Chemistry, University of Southern California, Los Angeles, California 90089-0482
[d] Department of Chemistry, Boston University, Boston, Massachusetts
[e] Department of Chemistry, Rice University, Houston, Texas, 77251-1892

[#]Authors contributed equally.
Authors to whom correspondence should be addressed: krylov@usc.edu, kluk@ibch.ru

Contents

I. EXPERIMENTAL DETAILS

The photoconversion of fluorescent proteins was studied using protein samples immobilized on TALON beads (Clontech) and *in cellulo* in live transiently expressing respective FPs HEK293T cells growing and visualizing in standard DMEM medium. To induce bleaching and redding and to quantify fluorescence the Leica AF6000 LX imaging system with Photometrics CoolSNAP HQ CCD camera was used. Green and red fluorescence images were acquired using 63× 1.4NA oil immersion objective and standard filter sets: GFP (excitation BP470/40, emission BP525/50) and TX2 (excitation BP560/40, emission BP645/75). Photoconversion was induced by irradiation with the GFP filter set using maximal light output (1 W/cm^2). LaserCheck (Coherent) power meter was used to measure total power of the

excitation light after the microscope objective. Light power density (W/cm^2) was estimated by dividing the total power by the area of the illuminated region.

For confocal microscopy, a Leica laser scanning confocal inverted microscope DMIRE2 TCS SP2 with an 63x 1.4NA oil objective and 125 mW Ar laser was used. Live HEK293 cells expressing target proteins in cytoplasm were imaged and bleached using the following settings: 512x512 points, zoom 16, 488 nm laser intensity 1.5 mkW ($\sim$150 W/cm^2) for detection and 120 mkW ($\sim$1200 W/cm^2) for bleaching, fluorescence detection at 500-550 nm.

Photoactivation was performed in a cyclic manner (a cycle consists of the red signal measurement, green signal measurement, and photoactivation). In widefield experiments exposure time for each cycle were 0.5-5 s (15-45 cycles depending on mutant). Time between cycles typically stated 2-2.3 s and composed of filter set change time (circa 2 s) plus red and green signals detection time (50-300 ms). Thus, the experimentally determined yield of redding is not the quantum yield, but the cumulative yield. It is defined as maximal red signal obtained after photoactivation (the height of kinetic curve plateau). The green form can either be converted to a bleached state or to the red chromophore. "Bleaching" is defined as the disappearance of the green signal — the intensity of the green fluorescence signal normalized to the initial green fluorescence:

$$Bleaching = \frac{I_{fl}^{Green}(t)}{I_{fl}^{Green}(t=0)} = 1 - \frac{N^{Red}(t)}{N_0} - \frac{N^{Bl}(t)}{N_0} = 1 - \frac{I^{Red}(t)\epsilon^{Green}Y_{fl}^{Green}}{I^{Green}(t=0)\epsilon^{Red}Y_{fl}^{Red}} - \frac{N^{Bl}(t)}{N_0}. \tag{1}$$

Since we do not know extinction coefficients, we cannot directly measure the amount of the bleached form, only the total decay of the green form.

"Redding" is defined as the appearance of the red form. It is the intensity of the red fluorescence signal depending on the number of photoactivation cycles (accumulated red signal due to photoconversion minus bleaching of the red form, etc). The red signal is normalized either to the maximal red signal value:

$$Redding = \frac{I_{fl}^{Red}(t)}{I_{fl,max}^{Red}(t')}, \tag{2}$$

where $I_{fl,max}^{Red}$ is a maximum value of the red fluorescence signal reaching during time-lapse series, or to the initial green signal value (Figs. 2b, S3; both signals are background-corrected):

$$Redding = \frac{I_{fl}^{Red}(t)}{I_{fl}^{Green}(t=0)}, \tag{3}$$

where $I_{fl}^{Red}(t)$ is the intensity of the fluorescence signal depending on the number of photo activation cycles (accumulated red signal due to photoconversion, bleaching of the red form, etc). Unfortunately, we do not know extinction coefficients or the amount of green form present. In YFPs, the main form also contributes to the red signal. This complication can be tackled differently, which gives somewhat different red form appearance curves; however, the main trends remain unchanged. The red form is not very stable and can also be bleached, which affects cumulative yields.

We also performed experiments under the anaerobic conditions. We found that bleaching and redding signals are essentially unaffected by the presence of oxygen under our conditions,

as illustrated below.

EGFP and EYFP can undergo reversible bleaching. The kinetics of reversible bleaching under low-intensity illumination in several variants of EGFP (i.e., EYFP, Citrine, eCFP) was investigated in Ref. [1]. It was found that these FPs undergo reversible bleaching; the fluorescence recovers spontaneously with time constants of 25-58 s. To address possible contribution of reversible bleaching into the bleaching signal, we repeated the measurements for EYFP and EGFP with 60 s intervals between the exposures. The kinetics was essentially unaffected. We estimated that the contribution of the reversible bleaching to the total bleaching signal does not exceed 10 %.

II. EXPERIMENTAL RESULTS

A. Spectral properties of EGFP, EYFP, and their mutants

TABLE S1: Properties of green/yellow absorption peak of EGFP, EYFP, and their mutants at position 145.

Protein	Absorption max, nm	Extinction coefficient, $M^{-1}cm^{-1}$
EGFP	488	55000
EGFP-Y145F	486	82000
EGFP-Y145L	490	15000
EYFP	515	84000
EYFP-Y145F	514	95000
EYFP-Y145L	514	16000

B. Bleaching and redding kinetics

We observe that at our conditions, both the bleaching and redding yields are very small in the absence of the oxidant; they increase at higher concentrations. The normalized yields are given in the main text (Fig. 2). The yield of the red form in Fig. 2 of main text was computed from the kinetics data as follows. After one irradiation cycle with arc-lamp (GFP filter set), the remaining green fluorescence (normalized according to the initial value, see Eq. (1)) and originating red fluorescence (normalized according to the maximal value, see Eq. (3)) were measured and shown in the graph. Each data point is an average of three independent experiments. The important result is that the green and red signals correlate with each other suggesting that bleaching is due to photooxidation and that photooxidation leads to the formation of the precursor of the red form.

Figs. S1 and S2 illustrate the effect of halide's size on the redding kinetics and the yield of the red form in EYFP. The yields are inversely proportional to halide ionic radii. Fig. S3 shows that redding could not be turned on by the chromophore protonation state change itself (upper panel), hoverer, redding efficiency is strongly increased at high pH and in the presence of halide (lower right panel). These data suggest that halides' ability to turn on EYFP redding is not related to their ability to slightly shift chromophore's protonation equilibrium (previously described by Wachter *et al.* [2]). On the other hand, in

the presence of halides, redding is more efficient under the conditions favoring deprotonated chromophores, in agreement with previous reports on GFP redding[3].

Fig. S4 shows the temperature dependence of the bleaching and redding kinetics in EGFP. In line with theoretical predictions, the rates of bleaching and redding increase at elevated temperature.
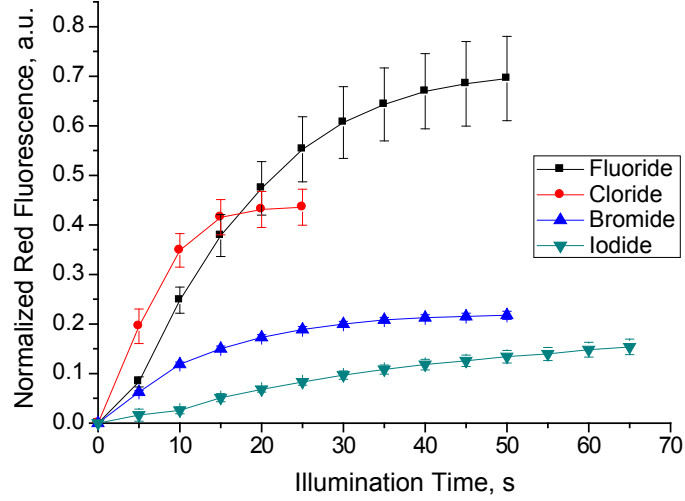

FIG. S1: Kinetic curves of EYFP red form production during cyclic photoactivation with epifluorescent microscope in presence of different halides. Redding was induced at the identical conditions in the presence of 150 mM of each ion.
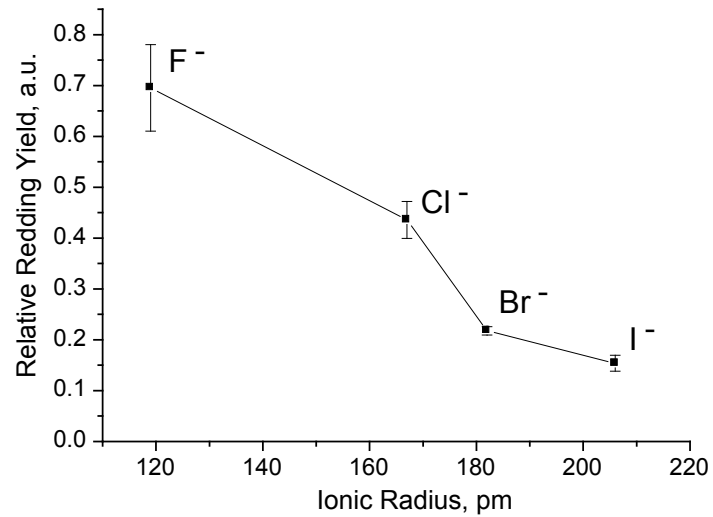
FIG. S2: Dependence of EYFP redding yield on the presence of different halide anions as a function of their respective ionic radii.
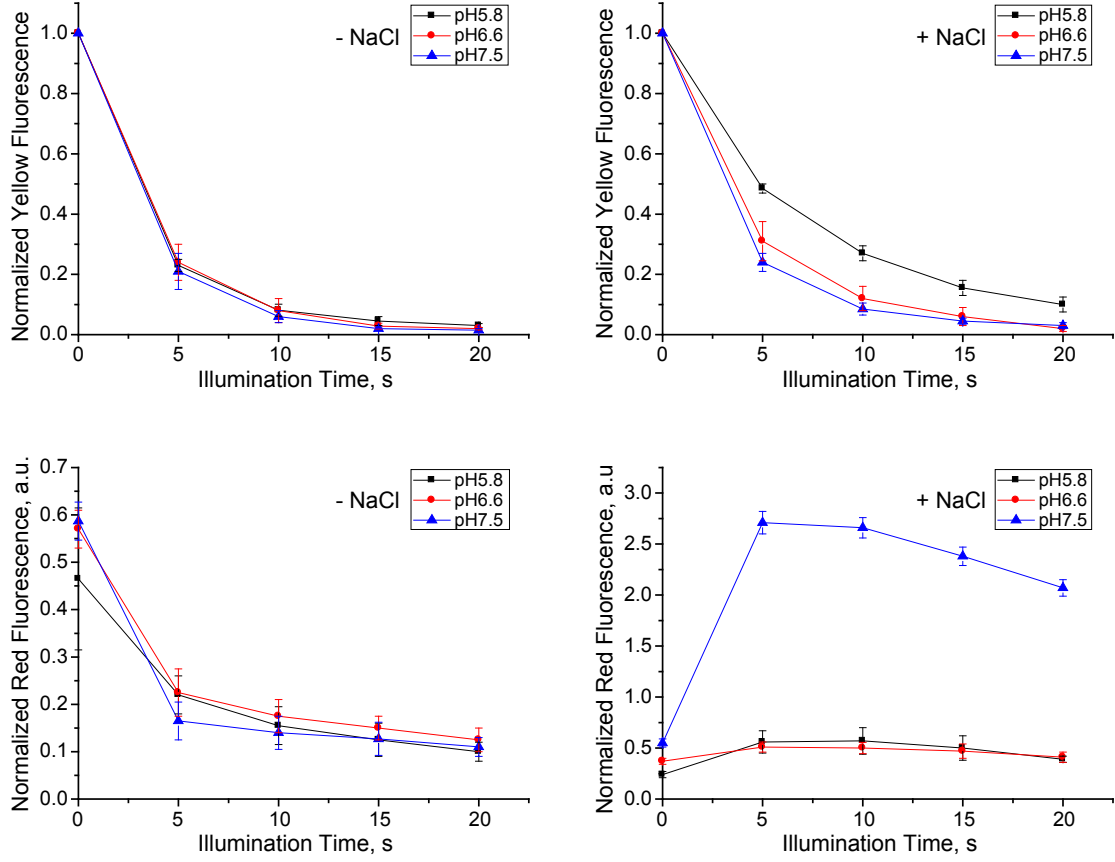
FIG. S3: EYFP bleaching (top) and redding (bottom) pH dependence in the absence (left column) and presence (right column) of 150 mM chloride anions.

C.   Aerobic versus anaerobic conditions

Fig. S5 compares EGFP bleaching kinetics at the aerobic and anaerobic conditions. Overall, the differences are small (relative to other factors) at present conditions, in particular, in the presence of oxidant (right panel). In presence of oxidant, without Cl$^-$(right panel), EYFP is more photostable. Note that with chloride and in the presence of oxidant, the aerobic and anaerobic kinetics (green and purple curves on the right panel) are indistinguishable. Without oxidant and with chloride, EYFP is more photostable at anaerobic conditions (purple and green curves on the left panel), which agrees with previous studies of the effect of oxygen on photostability of FPs[4, 5].
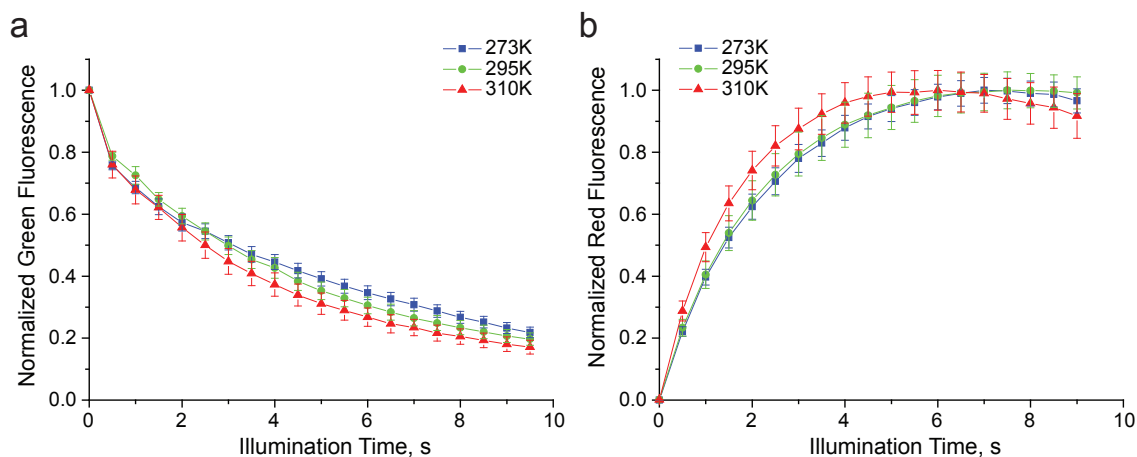
FIG. S4: Temperature dependence of bleaching (a) and redding (b) kinetics in EGFP.
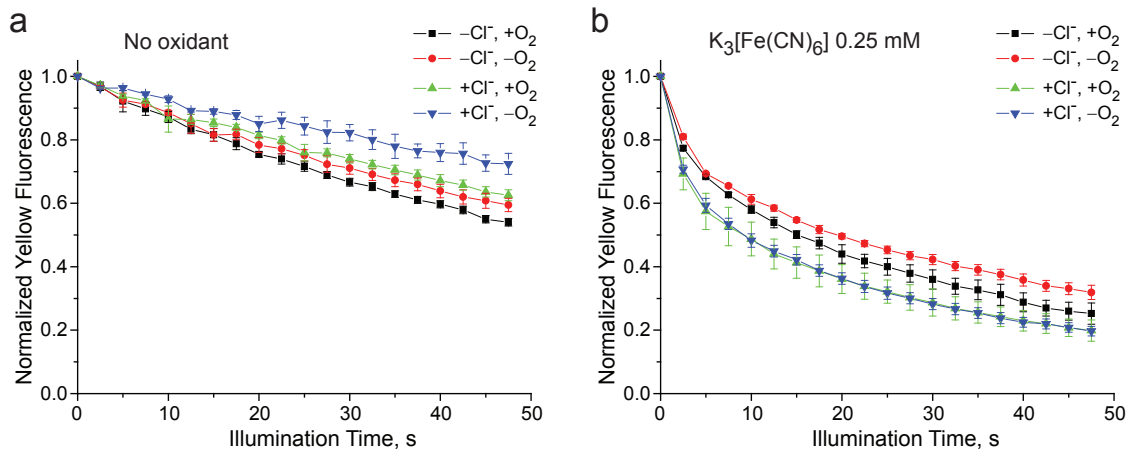
FIG. S5: Influence of oxygen and chloride anion on EYFP bleaching. Immobilized EYFP protein was illuminated in aerobic and anaerobic conditions in the absence (a) and presence (b) of potassium ferricyanide. $+Cl^-$ and $-Cl^-$ denote the experiments with and without the halide, respectively. Similarly, $+O_2$ and $-O_2$ mark the aerobic and anaerobic conditions. Mean and standard deviation for three independent experiments are shown.

III.   THEORETICAL METHODS AND COMPUTATIONAL DETAILS

A.   Marcus theory for electron-transfer rates and linear response approximation
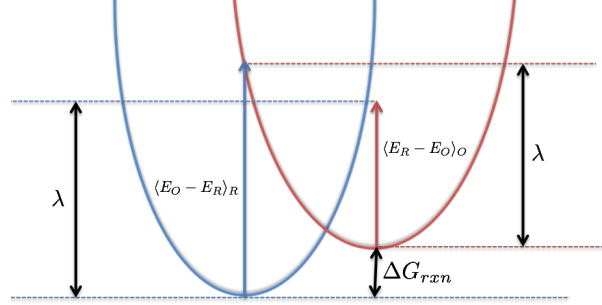
FIG. S6: Gibbs free energy curves and definitions of the key quantities in Marcus theory of electron transfer. O and R denote oxidized and reduced states, respectively.

Marcus theory of electron transfer (ET) gives the following rate expression[6, 7]:

$$k_{ET} = \frac{2\pi}{\hbar} |H_{DA}|^2 \frac{1}{\sqrt{4\pi\lambda k_B T}} \exp\left\{ -\frac{(\Delta G + \lambda)^2}{4\lambda k_B T} \right\}, \tag{4}$$

where ΔG, λ, and H_{DA} are the free energy change, reorganization energy, and coupling between the electronic states involved in ET. The definitions of these quantities are given in Fig. S6. ΔG is the overall thermodynamic drive for ET, reorganization energy λ is related to an effective barrier for ET, and H_{DA} is an electronic coupling between the ground and charge-transfer (CT) states.

In the limit of strong coupling, the ET proceeds in the adiabatic regime such that a single passage over the activation barrier completes ET[8]. In this regime, the Marcus expression is modified as follows:

$$k_{ET} = k_0 \exp\left\{ -\frac{(\Delta G + \lambda)^2}{4\lambda k_B T} \right\}, \tag{5}$$

with pre-exponential factor $k_0 \approx 10^{12} - 10^{13}$ s^{-1}. The pre-exponential factor in transition-state theory is: $k_0 = \frac{k_B T}{h} = 6.2 \times 10^{12}$.

Calculating ΔG and λ for a redox reaction by using linear response approximation. The difficulty in computing parameters for the Marcus rate expression is that one needs to go beyond electronic energies and deal with free energies. We use linear response approximation (LRA)[9, 10] to compute free energy and reorganization energy. ΔG of a reaction is related to the partition functions of the initial and final states as $\Delta G = -k_B T \ln \frac{Q_f}{Q_i}$; this expression can be rewritten as a relation between the free energy and the ensemble average of energy difference (ΔE):

$$\Delta G = -k_B T \ln \left\langle \exp\left(-\Delta E / k_B T \right) \right\rangle_i, \tag{6}$$

By truncating this expression after the first term, two expressions for oxidized and reduced state are obtained: $\Delta G = \langle \Delta E \rangle_R$ and $\Delta G = \langle \Delta E \rangle_O$. Combining these two expressions, we

obtain the LRA expression for free energy and reorganization energy:

$$\Delta G_{ox} = \frac{1}{2}\left(\langle E_O - E_R \rangle_R + \langle E_O - E_R \rangle_O\right), \tag{7}$$

$$\lambda_{ox} = \frac{1}{2}\left(\langle E_O - E_R \rangle_R - \langle E_O - E_R \rangle_O\right). \tag{8}$$

We use the following protocol to compute these quantities. First, we run MD for the initial (Chro$^-$) and oxidized (Chro$^\cdot$) states of the protein to generate equilibrium sampling (see Section III D). We then follow with the QM/MM calculations of VIE on both states, where VIE is defined as $VIE = E_O - E_R$. The detailed protocol is described in Section III E 1.

Calculating ΔG and λ for a charge-transfer reaction by LRA. In the context of ET, the oxidized state (O) and the reduced state (R) defined above refer to the CT and ground states, respectively. By replacing O by CT (for the charge-transferred state) and R by g (for the ground state), we apply LRA to ET processes by computing the energies of the CT states on the ground-state and CT surfaces. In our system, the CT state corresponds to ET from the chromophore to a tyrosine residue:

$$\Delta E_{CT} = VIE_{chr^-} + VEA_Y + E_{coul} \approx VIE_{chr^-} + VEA_Y. \tag{9}$$

Since only either donor or acceptor is charged in both states, we neglect the Coulomb interaction term between Chro and Tyr. The expressions for free energy and reorganization energy of charge transfer are as follows:

$$\Delta G_{CT} = \frac{1}{2}\left(\langle \Delta E_{CT} \rangle_g + \langle \Delta E_{CT} \rangle_{CT}\right) \tag{10}$$

$$\lambda_{CT} = \frac{1}{2}\left(\langle \Delta E_{CT} \rangle_g - \langle \Delta E_{CT} \rangle_{CT}\right), \tag{11}$$

where $\Delta E_{CT} \equiv E_{CT} - E_g$. The terms in Eqns. (10) and (11) can be computed as the vertical ionization and electron attachment energies (VIE and VEA) of the donor (chromophore) and acceptor (tyrosine), respectively. These expressions and the sign convention are the same as in Refs. [11–13].

We use the following protocol to compute these quantities. First, we run MD for the ground (Chro$^-$ ...Tyr) and CT (Chro$^\cdot$ ...Tyr$^-$) states to generate equilibrium sampling (see Section III D). We then follow with the QM/MM calculations of VIE, VEA, and the couplings. The detailed protocol is described in Section III E.

B. The Pathways model

To narrow down possible intermediate electron acceptors, we applied the *Pathways* model[14, 15] in which the tunneling probability (T_{DA}) between the specified donor and acceptor moieties is given by:

$$T_{DA} = K \prod_C \epsilon_C \prod_H \epsilon_H \prod_S \epsilon_S \tag{12}$$

where C, H, and S refer to the pathways through covalent bonds, H-bonds, and space, respectively. ϵ_C, ϵ_H and ϵ_S are empirical factors given by:

$$\epsilon_C = 0.6, \tag{13}$$

$$\epsilon_H = \epsilon_C^2 e^{-1.7(R-2.8)}, \tag{14}$$

$$\epsilon_S = \epsilon_C e^{-1.7(R-1.4)}, \tag{15}$$

which take into account that tunneling through the covalent bonds is more efficient than through the hydrogen bonds, etc.

C. Docking calculations

To evaluate the distances between an outside oxidant and selected residues, we performed docking calculations using *AutoDock*[16]. The starting point was the pdb structure to which we added hydrogens, according to the protonation states, and optimized the resulting structure. We used para-benzoquinone (BQ) as a model oxidant (structure optimized by ωB97X-D/cc-pVTZ) and analyzed its docking to EGFP, EYFP, and halide-bound EYFP. In these calculations, we considered a box (22.5×22.5×22.5 Å) around Tyr145. This box covered the volume around chromophore, Tyr145, and Tyr203. The *AutoDock* software[16] then determined 20-100 lowest-energy docking sites within this box.

We note that the differences in binding energies between different docking sites (as calculated by *AutoDock*) were less than 1 kcal/mol for the set of 100 lowest structures (energy difference of 1 kcal/mol at 298 K leads to Boltzmann population of about 20%). Several clusters of structures identified in these calculations are discussed in Section IV D.

To verify the results of the docking simulations, we performed MD simulations for the docked structure of EGFP with the shortest chromophore-BQ distance. The force-field parameters used for the BQ MD simulations were obtained as follows. The ωB97X-D/aug-cc-pVTZ NBO point charges[17] for the neutral form have been used. Equilibrium bond lengths and valence angles were taken from the gas-phase equilibrium ωB97X-D/aug-cc-pVTZ geometry. Force constants and van der Waals parameters were taken from the CHARMM General Force Field parameters for phenol. We then performed equilibrium simulations in the ground state (deprotonated chromophore, neutral Tyr145, neutral BQ) for 10 ns using the first 5 steps, as described below in Sec. III D. We then analyzed the distance between BQ and Tyr145 by computing the distances between one selected aromatic carbon of Tyr145 and BQ (see Fig. S7). We observed that the distance between Tyr145 and BQ stays mostly within 3.9-5.4 Å, for a 10 ns long MD trajectory. The average distance and the standard deviation are 4.63 Å and 0.46 Å, respectively. The averaging is performed using 4,000 snapshots along the trajectory.

D. MD and QM/MM setups

1. *Preparation of systems for MD and QM/MM simulations*

Molecular dynamics. CHARMM27 parameters for standard protein residues[18] and the parameters derived by Reuter *et al.* for the anionic GFP chromophore were used in the MD calculations[19].
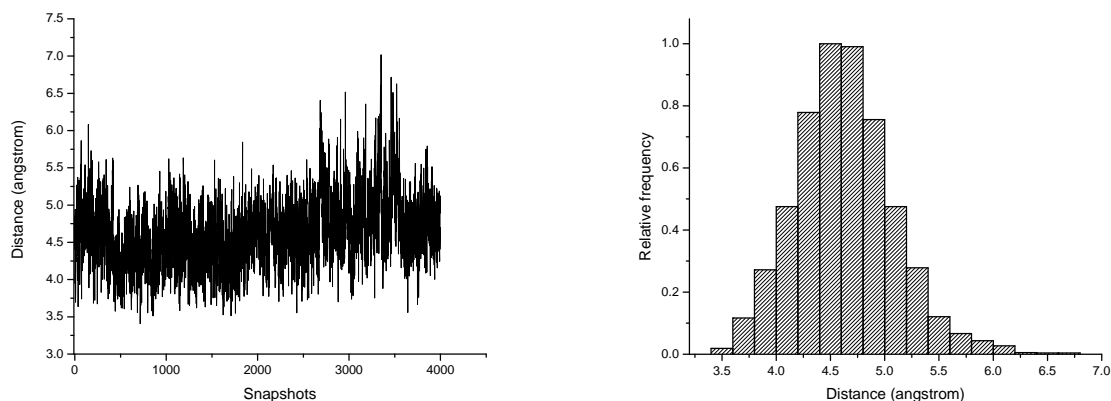
FIG. S7: Distance analysis between Tyr145 and BQ docked on the surface of EGFP along a 10 ns trajectory. Graphs show fluctuations in the relative distance along the trajectory (left) and the resulting distribution (right). The snapshots were taken every 2.5 ps.

Parameters for the oxidized chromophore were obtained by adjusting the structural parameters and point charges using the following protocol based on the extrapolation between the reduced and oxidized structures. We first optimized the chromophore structure (transferred from Dronpa) in the initial (anionic) and the oxidized (neutral radical) states while keeping the nearby residues (Arg62, Ser142, His193, Glu211, and three water molecules in Dronpa) fixed by using the constrained optimization feature. We then computed the difference between the NBO charges[17], bond lengths and bond angles for the two structures (anionic and neutral) obtained in the constrained optimization. To obtain the force-field parameters of the oxidized form, we modified the force-field parameters of the initial (anionic) chromophore by adding the difference between the two states computed from the constrained optimization calculations.

Using a similar protocol, we derived the parameters for the reduced (electron-attached) state of Tyr based on the CHARMM27 parameters of the neutral form. Constrained optimization of Tyr203 (in EYFP) was performed at the fixed geometry of a cluster comprising Val150, Val224, Glu222, Leu201, Gln69, and two nearby water molecules. The same parameters were used for Tyr145. Relevant NBO charges for Tyr were obtained from the gas-phase optimization. We only changed charges, bond lengths and bond angles for the oxidized chromophore and reduced Tyr relative to the respective reference parameters.

The TIP3P water model was used to describe explicit solvent around protein. Since CHARMM27 only has parameters for chloride, the iodide from the X-ray structures was replaced by Cl^-. The protein was solvated in a box producing a water buffer of about 15 Å. The surface charges were neutralized with Na^+ and Cl^- ions at appropriate places. The MD calculations were performed on these systems as follows:

1. Minimization for 2000 steps with 2 fs time step prior to adding water box.

2. Minimization for 2000 steps with 2 fs time step of the solvated structure.

3. Equilibration of the solvent using periodic boundary condition (PBC) with 1 fs time step for 500 ps (protein structure is frozen, only solvent was allowed to relax).

4. Equilibration run for 2 ns with 1 fs time step with PBC in which the whole system was allowed to move under constant pressure and temperature (NPT ensemble).

5. Production run for 2 ns with 1 fs time step with PBC.

6. The snapshots for the QM/MM calculations were collected from the production run.

The MD simulations were performed using *NAMD* in isobaric-isothermal ensemble with Langevin dynamics[20]. Pressure and temperature used for the simulations were 1 atm and 298 K. All simulations were performed with rigid-bond option of *NAMD* keeping the OH bonds frozen.

Protein structures and protonation states. We used X-ray structures by Watcher of EYFP-H148Q for EYFP with and without iodide anion[21]. The structures were obtained from the protein data bank with pdb id 1F0B and 1F09 for EYFP without and with iodide anion, respectively[21]. For GFP, we used 1EMA structure[22].

Protonation states for all proteins were checked with *Propka software* first and then the residues around the chromophore were checked manually, as described below. *Propka* suggested that Glu222 should be protonated in both proteins. We performed dynamics on two protonation states for both EYFP structures. The two possible protonation states for EYFP are:

1. GLU 222: Deprotonated form of GLU 222

2. GLUP 222: Protonated form of GLU 222

We ran a 2 ns trajectory for both protonation states of the the two EYFP structures and computed average hydrogen-bond distances. We then compared these distances with those from the X-ray structures. The protonated form of Glu222 yielded the best agreement. We protonated the oxygen that is closer to the chromophore (CR2 66); the other oxygen atom of Glu222, which is closer to Tyr203, was not protonated. In the protonated form, the hydrogen bond is formed between the carboxylic oxygen atom of Glu222 and N of imidazolinone ring.
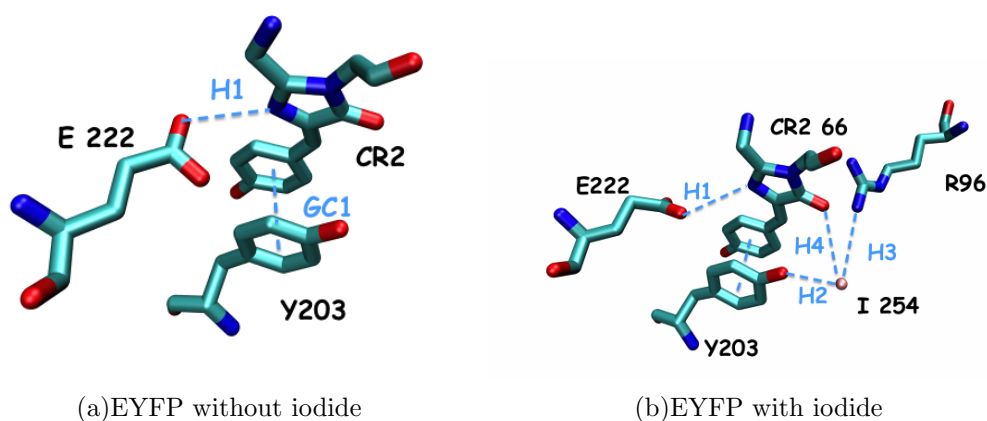

(a)EYFP without iodide   (b)EYFP with iodide

FIG. S8: Possible H-bonds around the chromophore in EYFPs without and with halide.

The π-stacked tyrosine (Tyr203) is not present in EGFP. In EGFP, deprotonated form of Glu222 needs to be considered since it can form hydrogen bond with the threonine-like

side chain of the EGFP chromophore in the deprotonated form (Fig. S9). The phenolate oxygen of the EGFP chromophore forms a hydrogen bond with nitrogen of His148. So we protonated the N-atom of His148 residue (HSD form) that is closest to chromophore. Arg96 may also form a hydrogen bond with the oxygen atom of the imidazolinone group of the EGFP chromophore. These protonation states are the same as in Ref. [23], except for Glu222, which was protonated in Ref. [23] but is deprotonated in our model.
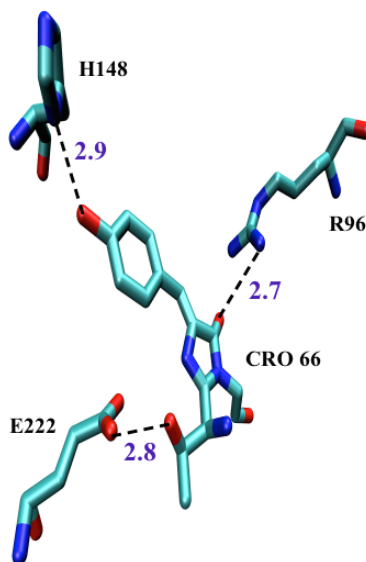
FIG. S9: Possible H-bonds around the chromophore in EGFP.

To check the effect of mutating the Tyr145 residue, we constructed EGFP-Y145L by mutating Tyr145 to Leu145 using *Mutator* plugin in VMD followed by the minimization of the mutated protein with the same force-field parameters described above.

2. QM/MM schemes

The VIE and the modified vertical ionization energy (mVIE) of the chromophore and modified VEA (mVEA) of the tyrosine residues were computed using the following QM/MM protocol (full details given in section III E 2).

In VIE/mVIE calculations (as well as in the calculations of excitation energies), only the chromophore was included in the QM part, as shown in Fig S12. In mVEA calculations, the QM part comprised the tyrosine residue (Fig. S13). For CDFT-CI calculations, both the chromophore and the tyrosine were included in the QM part. The rest of the system (protein+solvent) was treated as point charges.

Hydrogen atoms were added in the same direction (with the standard CH bond distance) at the QM border atoms to saturate their valences. The charges of the green and red-colored atoms in Figs. S12 and S13 were set to zero (the net neutralized charge of the red-colored atoms was equally redistributed over the rest of the atoms of that residue) to avoid overpolarization of the QM part due to the MM point charges at the QM-MM boundary.

The MD snapshots were converted to the QM/MM *Q-Chem* input file by using a *Python* script. *VMDTkconsole* was used to extract the frames from the MD trajectories. We observe that the convergence with respect to the number of snapshots is achieved relatively fast. In our production calculations, 41 snapshots were used for averaging.

The convergence of the redox parameters with respect to the number of snapshots has been studied in detail in Ref. [24]. They reported the values of thermodynamic parameters obtained by using 50 snapshots, however, based on their data, the convergence was achieved at 20 snapshots[24]. We observed fast convergence for the redox parameters ($\sim$20 snapshots), however, the respective quantities for the ET reactions require more extensive sampling.

Fig. S10 illustrates the convergence of thermodynamic averaging in our calculations. As follows from Eqns. (25) and (26), the convergence of ΔG and λ is driven by $\left\langle \Delta E'_{cdftci} \right\rangle_g$ and $\left\langle \Delta E'_{cdftci} \right\rangle_{CT}$. These quantities for EYFP are shown in Fig. S10. We chose EYFP (without halide) as a representative system because it shows the slowest convergence, i.e., when we increased the number of snapshots from 19 to 41, the highest change in the ET rates was observed for this system, whereas the rates for EGFP were essentially converged at 19 snapshots.
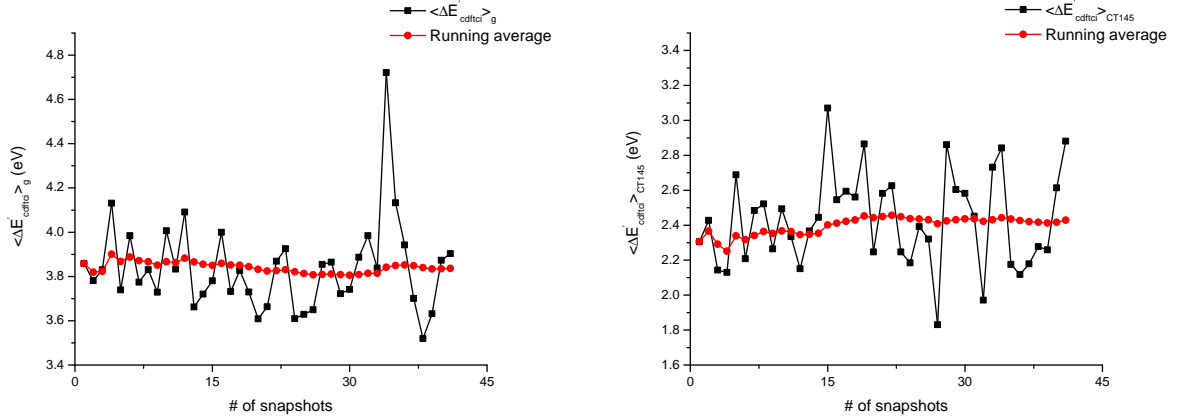
FIG. S10: Convergence of $\left\langle \Delta E'_{cdftci} \right\rangle_g$ and $\left\langle \Delta E'_{cdftci} \right\rangle_{CT}$ for EYFP without halide with Tyr145 as the intermediate acceptor.

We also checked the convergence of the electronic coupling values in EGFP along the ground-state trajectory. We observed that after about 25 snapshots the coupling values are essentially converged (see Fig. S11).

mVIEs, mVEAs and couplings were calculated at the ωB97X-D/aug-cc-pVDZ, ωB97X-D/aug-cc-pVTZ and ωB97X-D/cc-pVDZ levels of theory[25, 26]. Since the side chains of EGFP were always in the QM part, the charge distributions at QM-MM boundary in the mVIE and mVEA calculations were identical.

Three QM/MM schemes were used in EGFP calculations:

1. QM - Chromophore for VIE/mVIE

2. QM - Tyr145 for mVEA

3. CDFT-CI: QM - Chromophore + Tyr145
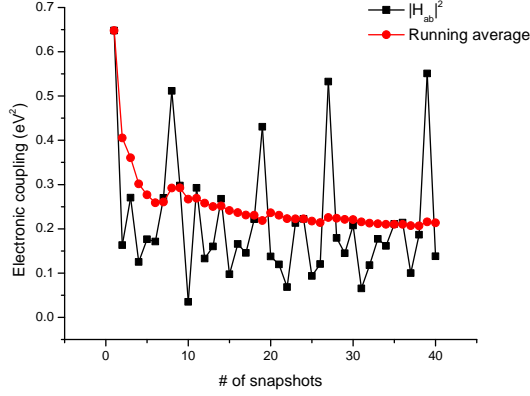
FIG. S11: Convergence of the Chro-Ty145 coupling in the ground state of EGFP.

Five QM/MM schemes were used in EYFP calculations:

1. QM - Chromophore for VIE/mVIE

2. QM - Tyr145 for mVEA

3. QM - Tyr203 for mVEA

4. CDFT-CI: QM - Chromophore + Tyr145

5. CDFT-CI: QM - Chromophore + Tyr203

To validate our QM/MM schemes, we computed excitation energies using SOS-CIS(D)/aug-cc-pVDZ and compared them with the experimental absorption energies. We observe excellent agreement between the computed and experimental values of excitation energies, the largest error being 0.18 eV for the halide-bound EYFP.

TABLE S2: Comparison between the computed (SOS-CIS(D)/aug-cc-pVDZ) and experimental excitation energies (eV). Only the chromophore is included in the QM part and the rest of the protein and solvent was treated as point charges. Computed values were averaged over 19 snapshots.

System	Computed	Experimental
EGFP	2.55	2.54
EYFP	2.55	2.41
EYFP + Cl$^-$	2.59	2.41

E. Protocols for calculating energetics and couplings

1. Relevant energies for chromophore oxidation and redox potentials

The Gibbs free energy of the ground-state chromophore oxidation can be computed using LRA as specified by Eqns. (7) and (8) where $E_O - E_R \equiv VIE$. ΔG_{ox} in the excited state
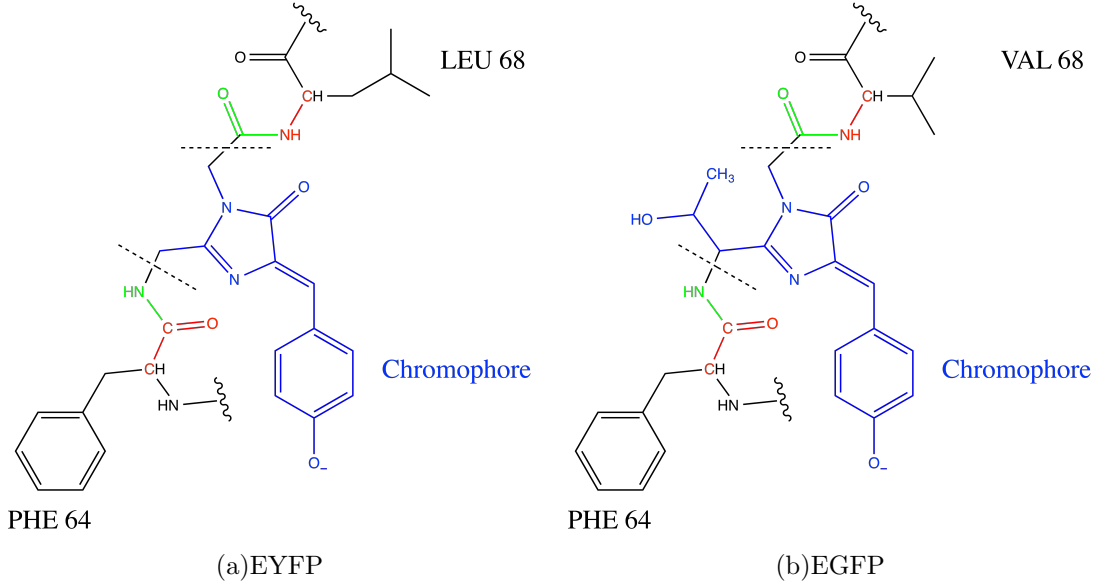
FIG. S12: QM/MM schemes for EYFP and EGFP used in the mVIE calculations of the chromophore. The black dotted lines denote the boundary between the QM (blue) and MM parts. The MM part in which point charges were set to zero is denoted by green and red. Green atoms are part of the chromophore. Note that the QM part does not contain all atoms of the chromophore.
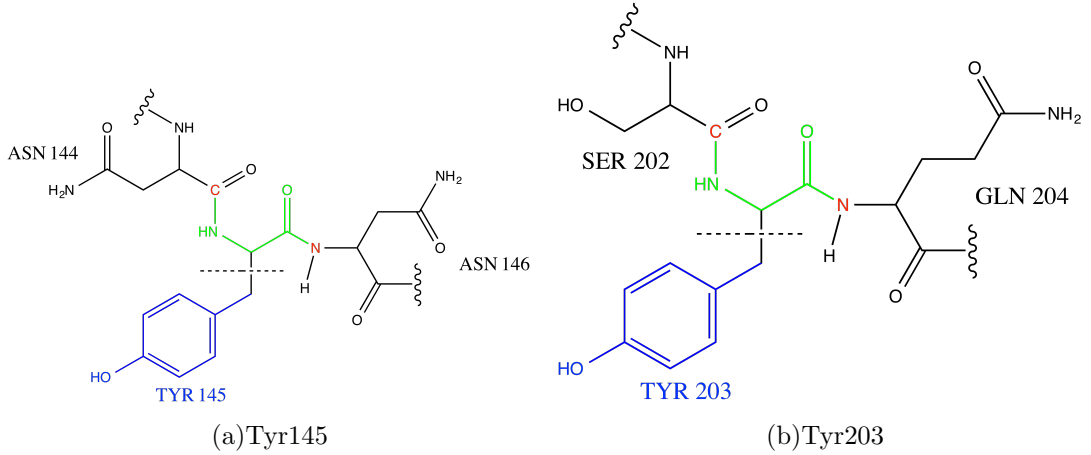
FIG. S13: QM/MM scheme for EYFP and EGFP used in the mVEA calculations of tyrosines. The black dotted lines denote the boundary between the QM (blue) and MM parts. The MM part in which point charges were set to zero is denoted by green and red. Green atoms are part of respective tyrosine residues. Since the residues around those tyrosines are the same in EGFP and both EYFPs, the same QM/MM scheme was used for all proteins. Note that the QM part does not contain all atoms of the tyrosine residue.

was computed as follows:

$$\Delta G_{ox}^{ex} = \Delta G_{ox}^{gs} - E_{em} \tag{16}$$

We computed VIE of the chromophore on the ground-state and oxidized chromophore surfaces for all three proteins. From Eqns. (7) and (16) we obtained the free energies of

oxidation of the chromophore in the S_0 and S_1 states. The oxidation potential was calculated from the free energy of oxidation of the ground state as $\Delta G_{ox}^{gs} = -nFE_{ox}$ ($n=1$ for one-electron oxidation). To compute the standard oxidation potential with respect to standard hydrogen electrode (SHE), we used $\Delta G(SHE)=4.28$ eV (see Ref. [27]).

TABLE S3: Redox properties of the chromophores of EGFP, EYFP and halide-bound EYFP. VIEs of the chromophores on the reduced (ground) and oxidized surfaces were averaged over 41 snapshots using ωB97X-D/aug-cc-pVDZ. Energies are in eV and the reduction potentials are in V with respect to SHE.

System	$<VIE>_{red}$	$<VIE>_{ox}$	ΔG_{ox}^{gs}	λ_{ox}	E_{em}^{expt}	ΔG_{ox}^{ex}	E_{red}^0 vs. SHE (V)
EGFP	6.149	2.952	4.551	1.599	2.44	2.111	0.27
EYFP	6.097	3.297	4.697	1.400	2.35	2.347	0.42
EYFP + Cl$^-$	5.960	2.588	4.274	1.686	2.35	1.924	-0.01
EGFP-Y145L	6.076	3.020	4.548	1.528	2.44	2.108	0.27

2. Relevant energies for the CT states

In the calculations of the free energies for the CT process, Eqns. (7) and (8) need to be modified accounting for the fact that the electron does not leave the protein, but is transferred to another residue (acceptor). Ideally, we would prefer to compute the energy of the CT state by a CDFT-CI calculation in which both diabatic states, the ground and the CT state, are prepared explicitly and ΔE_{CT} is computed from the energy difference of those two states. However, due to the convergence issues of CDFT-CI with augmented bases, we employed an extrapolation scheme in which CDFT-CI energies obtained in a small basis set were corrected by VIE and VEA of the donor and acceptor computed using large bases.

We begin by computing ΔE_{CT} as follows:

$$\langle \Delta E_{CT} \rangle_g = \left\langle E_{chr\cdot}^A - E_{chr-}^A + E_{A^-}^{chr^-} - E_A^{chr^-} \right\rangle_g, \tag{17}$$

$$\langle \Delta E_{CT} \rangle_{CT} = \left\langle E_{chr\cdot}^{A^-} - E_{chr-}^{A^-} + E_{A^-}^{chr\cdot} - E_A^{chr\cdot} \right\rangle_{CT}, \tag{18}$$

where A is an acceptor, which is neutral in the ground state and negatively charged in the CT state. The subscript was taken in QM and superscript was taken in MM with other point charges. Eqns. (17) and (18) treat the problem as an independent redox problem for the donor and the acceptor because the change in the charge distribution of the acceptor is not accounted for.

As the next step, we compare $< \Delta E_{CT} >$ with the CDFT-CI results. For that, we modify Eqns. (17) and (18) as follows:

$$\langle \Delta E_{CT} \rangle_g = \left\langle E_{chr\cdot}^{A^-} - E_{chr-}^A + E_{A^-}^{chr\cdot} - E_A^{chr^-} \right\rangle_g \tag{19}$$

$$\langle \Delta E_{CT} \rangle_{CT} = \left\langle E_{chr\cdot}^{A^-} - E_{chr-}^A + E_{A^-}^{chr\cdot} - E_A^{chr^-} \right\rangle_{CT} \tag{20}$$

Note the subtle difference between Eqns. (17) and (19) and Eqns. (18) and (20) — in the modified definition the sum of charges on the chromophore and the acceptor is always -1 while computing these terms. Now the difference, $\delta E_{corr,i} = \langle \Delta E_{CT}^{cc-pVDZ} \rangle_i - \langle \Delta E_{cdftci}^{cc-pVDZ} \rangle_i$,

arises from the orbital overlap and the Coulomb contribution as well as a small contribution from the adjustment of charges around the QM region in the CDFT-CI calculations.

We performed CDFT-CI calculations using ωB97X-D/cc-pVDZ. We also computed ΔE_{CT} at the same level using Eqns. (19) and (20) and at a higher level of theory (using aug-cc-pVTZ and aug-cc-pVQZ bases and the CBS extrapolation). In mVIE calculations of the chromophore, the ωB97X-D/aug-cc-pVDZ values are essentially converged (no difference relative to the ωB97X-D/aug-cc-pVTZ values); thus, these values were used without extrapolation to CBS. Thus, in extrapolation of ΔE_{CT} to the CBS limit, only mVEA of the acceptor was extrapolated.

We used two-point extrapolation scheme to obtain mVEA at the ωB97X-D/CBS level using mVEA computed by ωB97X-D/aug-cc-pVTZ and ωB97X-D/aug-cc-pVQZ. We subtracted the correction term (obtained at the ωB97X-D/cc-pVDZ level) from ΔE_{CT} computed at the CBS limit. The VEA or mVEA of tyrosine was defined as: $VEA_{tyr} = E_{tyr^{\cdot-}} - E_{tyr}$. Both energies were extrapolated to the CBS limit using $E(X) = E_{CBS} + AX^{-3}$ and $E(Y) = E_{CBS} + AY^{-3}$, where $E(X)$ and $E(Y)$ are the energies obtained with the aug-cc-pVTZ ($X = 3$) and aug-cc-pVQZ ($Y = 4$) basis sets, respectively. This was repeated for all frames.

With these modifications of Eqns. (10) and (11), the final expressions for the free energy and reorganization energy of charge transfer become:

$$\Delta G_{CT} = \frac{1}{2}\Bigg(\Big\langle E_{chr^{\cdot}}^{A^{-}} - E_{chr^{-}}^{A} + E_{A^{-}}^{chr^{\cdot}} - E_{A}^{chr^{-}} \Big\rangle_g - \delta E_{corr,g}$$

$$+ \Big\langle E_{chr^{\cdot}}^{A^{-}} - E_{chr^{-}}^{A} + E_{A^{-}}^{chr^{\cdot}} - E_{A}^{chr^{-}} \Big\rangle_{CT} - \delta E_{corr,CT} \Bigg), \tag{21}$$

$$\lambda_{CT} = \frac{1}{2}\Bigg(\Big\langle E_{chr^{\cdot}}^{A^{-}} - E_{chr^{-}}^{A} + E_{A^{-}}^{chr^{\cdot}} - E_{A}^{chr^{-}} \Big\rangle_g - \delta E_{corr,g}$$

$$- \Big\langle E_{chr^{\cdot}}^{A^{-}} - E_{chr^{-}}^{A} + E_{A^{-}}^{chr^{\cdot}} - E_{A}^{chr^{-}} \Big\rangle_{CT} - \delta E_{corr,CT} \Bigg). \tag{22}$$

Defining $mVIE_{chr^-} \equiv E_{chr^{\cdot}}^{A^{-}} - E_{chr^{-}}^{A}$ and $mVEA_A \equiv E_{A^{-}}^{chr^{\cdot}} - E_{A}^{chr^{-}}$, Eqns. (21) and (22) become:

$$\Delta G_{CT} = \frac{1}{2}\Bigg(\Big\langle mVIE_{chr^-} + mVEA_A \Big\rangle_g - \delta E_{corr,g}$$

$$+ \Big\langle mVIE_{chr^-} + mVEA_A \Big\rangle_{CT} - \delta E_{corr,CT} \Bigg), \tag{23}$$

$$\lambda_{CT} = \frac{1}{2}\Bigg(\Big\langle mVIE_{chr^-} + mVEA_A \Big\rangle_g - \delta E_{corr,g}$$

$$- \Big\langle mVIE_{chr^-} + mVEA_A \Big\rangle_{CT} - \delta E_{corr,CT} \Bigg). \tag{24}$$

To further simplify these equations, we define the term, $\big\langle \Delta E'_{cdftci} \big\rangle_i \equiv \big\langle mVIE_{chr^-} +$

$mVEA_A\rangle_i - \delta E_{corr,i}$, such that the above equations assume the following form:

$$\Delta G_{CT} = \frac{1}{2}\left(\left\langle\Delta E'_{cdftci}\right\rangle_g + \left\langle\Delta E'_{cdftci}\right\rangle_{CT}\right), \tag{25}$$

$$\lambda_{CT} = \frac{1}{2}\left(\left\langle\Delta E'_{cdftci}\right\rangle_g - \left\langle\Delta E'_{cdftci}\right\rangle_{CT}\right). \tag{26}$$

The *subscript* outside the ensemble average, $\langle...\rangle_i$, represents the surface on which the averaging was performed. Eqns. (25) and (26) compute the free energy change and reorganization energy involved in the ground-state CT process. But since we are interested in photoinduced ET, where the initial state is the excited state, we need to subtract E_{em} from ΔG_{CT} to obtain ΔG_{CT}^{ex} and λ_{CT}^{ex}:

$$\Delta G_{CT}^{ex} = \frac{1}{2}\left(\left\langle\Delta E'_{cdftci}\right\rangle_g + \left\langle\Delta E'_{cdftci}\right\rangle_{CT}\right) - E_{em}. \tag{27}$$

Note that $\lambda_{CT}^{ex} = \lambda_{CT}$ since from $\langle\Delta E'_{cdftci}\rangle_g - E_{em}$ and $\langle\Delta E'_{cdftci}\rangle_{CT} - E_{em}$, E_{em} cancels out while subtracting one from another to calculate reorganization energy.

We define:

$$\left\langle\Delta E'_{CT}\right\rangle_i = \left\langle mVIE_{chr^-}^{CBS} + mVEA_Y^{CBS}\right\rangle_i \tag{28}$$

$$\left\langle\Delta E_{CT}^{cc-pVDZ}\right\rangle_i = \left\langle mVIE_{chr^-}^{cc-pVDZ} + mVEA_Y^{cc-pVDZ}\right\rangle_i, \tag{29}$$

where i represents the surface on which these terms were computed. According to the definition, we also have, $\delta E_{corr,i} = \left\langle\Delta E_{CT}^{cc-pVDZ}\right\rangle_i - \left\langle\Delta E_{cdftci}^{cc-pVDZ}\right\rangle_i$ and we estimate the extrapolated energy difference between the ground and CT states as: $\left\langle\Delta E'_{cdftci}\right\rangle_i = \left\langle\Delta E'_{CT}\right\rangle_i - \delta E_{corr,i}$.

TABLE S4: Energy differences between the ground and CT states for 41 frames along the MD trajectory calculated on the ground-state surfaces. All values are in eV.

System	Acceptor	ωB97X-D/cc-pVDZ				Extrapolated
		$\langle\Delta E_{CT}\rangle_g$	$\langle\Delta E_{cdftci}\rangle_g$	$\delta E_{corr,g}$	$\langle\Delta E'_{CT}\rangle_g$	$\langle\Delta E'_{cdftci}\rangle_g$
EGFP	145	9.4065	5.6426	3.764	7.501	**3.737**
EYFP	145	9.2662	5.4965	3.770	7.607	**3.837**
	203	8.5109	5.0668	3.444	6.644	**3.200**
EYFP-Y145L	203	8.6687	5.2233	3.445	6.825	**3.380**
EYFP + Cl$^-$	145	8.9374	5.4130	3.524	7.221	**3.697**
	203	9.4811	5.4196	4.062	7.504	**3.442**

3. Calculations of electronic couplings between the CT states

Electronic couplings, H_{DA}, were calculated using CDFT-CI[13, 28–30]. The relevant states are: (i) Chro$^-$+Tyr (ii) Chro$^·$+Tyr$^-$. Thus, both residues were included in the QM part, and the rest of the system was described by point charges. The calculations were performed for several snapshots along the production-run trajectory at 298 K, unless

TABLE S5: Energy differences between the ground and CT states for 41 frames along the MD trajectory calculated on the CT-state surfaces. All values are in eV.

System	Acceptor	ωB97X-D/cc-pVDZ				Extrapolated
		$\langle\Delta E_{CT}\rangle_{CT}$	$\langle\Delta E_{cdftci}\rangle_{CT}$	$\delta E_{corr,CT}$	$\langle\Delta E'_{CT}\rangle_{CT}$	$\langle\Delta E'_{cdftci}\rangle_{CT}$
EGFP	145	2.0915	2.1531	-0.062	1.984	**2.046**
EYFP	145	3.0921	2.5891	0.503	2.932	**2.429**
	203	3.5220	2.8993	0.623	3.250	**2.627**
EYFP-Y145L	203	3.3647	2.8201	0.545	3.137	**2.592**
EYFP + Cl$^-$	145	2.1535	2.1785	-0.025	2.099	**2.124**
	203	4.7700	3.4647	1.305	4.277	**2.972**

specified otherwise. We also computed the coupling on the CT surface since they are needed for computing the reverse rate constants. In calculations of the Chro-Tyr92 couplings, additional mediating residues were included in the QM part, as shown in Fig. S14. In these calculations, the mediating residues obtained from the *Pathways* model calculations were chopped at appropriate positions (no peptide bonds) for keeping the system size to a reasonable one for all cases.
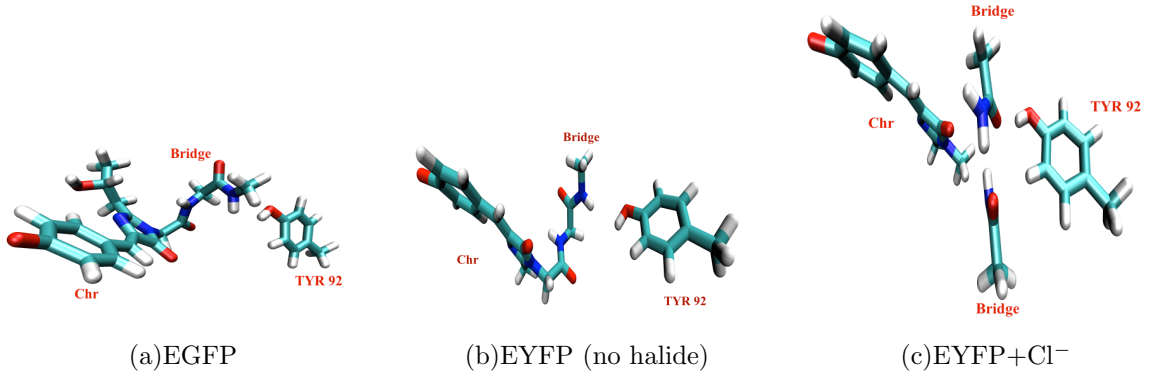

(a)EGFP   (b)EYFP (no halide)   (c)EYFP+Cl$^-$

FIG. S14: Residues included in QM in the calculations of the couplings between the chromophore and Tyr92, based on the *Pathways* model predictions.

IV. COMPUTATIONAL RESULTS

A. Relevant redox potentials

TABLE S6: Standard ΔG_{red} (eV) of selected oxidants.

OX species	ΔG_{red}(OX)	Source
O_2	-4.37	a
Cyt-c	-4.56	a
BQ	-4.30	b
BQ(res)	-1.80	c

a Estimated from E^0.

b Gas-phase AEA plus $\Delta\Delta G_{solv}$ by SM8 using M062X/6-31+G(*,*) at the ωB97X-D/cc-pVDZ geometry.

c Assuming electron attachment via the ^2A_u resonance state.

B. Possible intermediate electron acceptors: Energetics

The most likely electron acceptors[31] are aromatic residues such as tryptophan, tyrosine, phenylalanine, and histidine (see Fig. S15).
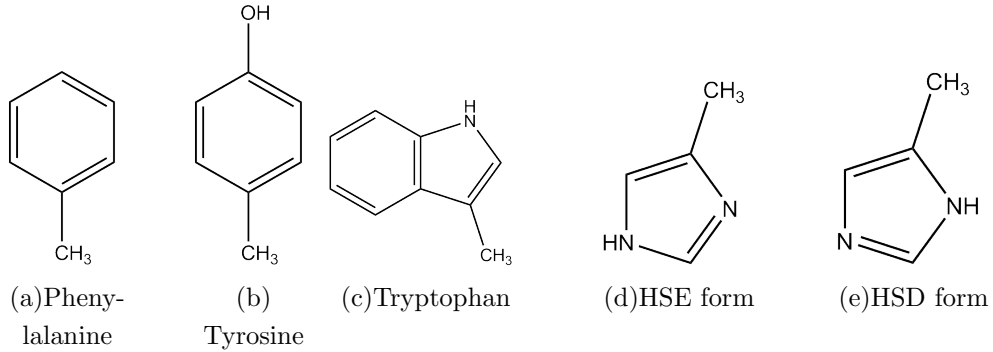
FIG. S15: Gas-phase structures of the aromatic groups of the amino acids that can serve as electron acceptors. Histidine has two neutral forms.

To estimate relative electron-accepting ability, we first consider gas-phase electron-attachment energies (EA); they are given in Table S7. As one can see, the gas phase EAs of these aminoacids are positive meaning that the respective anions would be unstable (in the stark contrast to benzoquinone, which is known to be an efficient oxidizing agent). In the protein (or solution), the anionic forms can be stabilized by electrostatic interactions. However, relative gas phase energetics are still useful for understanding their relative electron accepting ability, which is: Trp>Tyr>Phe>His.

TABLE S7: Gas phase EAs (eV) of tryptophan, tyrosine, histidine, phenylalanine, and benzo-quinone.

Residue	VEA	AEA
Phenylalanine	1.77	1.58
Tyrosine	1.70	1.48
Tryptophan	1.51	1.33
Histidine (HSE form)	2.97	2.61
Histidine (HSD form)	2.87	2.57
p-benzoquinone	-1.55	-1.86

EA≡E_{A^-}-E_A; negative values mean that A^- is lower in energy than A.
Structures (see Fig. S15) and energies: ωB97X-D/cc-pVTZ.

C. Pathway calculations

To narrow down possible intermediate electron acceptors, we begin with calculating tunneling probabilities (T_{DA}) using the *Pathways* model, as described in Section III B. We computed T_{DA} for all possible electron acceptors in EGFP. The results are summarized in Table S8. The computed values roughly correlate with the DA distances. Based on the data in Table S8, the most likely electron acceptors in EGFP are: Tyr145, Tyr92, Phe64, Phe165, and His148. Based on the corresponding EAs, we can neglect His148 and consider Tyr145 and Tyr92 as the most likely acceptors. Docking and couplings calculations presented below singled our Tyr145 as the most important intermediate electron acceptor.

TABLE S8: EGFP *Pathways* calculations: T_{DA} from chromophore to potential electron acceptors.

Acceptor	T_{DA}	Mediated by	Distance, Å
Tyr145	1.7×10^{-2}	through space	4.6
Tyr92	1.4×10^{-3}	Val68, Gln69	
Tyr143	6.2×10^{-5}	Tyr145	
Tyr151	7.3×10^{-4}	Val150	
Tyr200	1.4×10^{-4}	Val150, Leu201	
Tyr182	5.2×10^{-4}	Arg96, Gln183	
Phe46	1.2×10^{-3}	Phe64	
Phe64	7.8×10^{-2}		
Phe71	7.8×10^{-4}	Val68, Gln69, Cys70	
Phe84	2.5×10^{-4}	Gln69	
Phe165	1.1×10^{-2}	through space	3.77
Phe223	1.3×10^{-3}	Glu222	
His148	3.6×10^{-1}	through space	
Trp57	1.7×10^{-4}	Phe64	

As the next step, we compare T_{TA} in EGFP with those in EYFP (with and without chloride). The results are given in Table S9. The most important observations are: (i) T_{DA} to Tyr203 in EYFP is comparable to that for Tyr145; (ii) the chloride has a very small effect on all tunneling probabilities except for that to Tyr92 (chloride binding increases T_{DA} by a factor of 15). We then consider T_{DA} from Tyr203 to other possible acceptors (see Table S10).

We observe that these rates are not affected by Cl$^-$, except for Tyr92. We also note that although T_{DA} to Tyr145 is relatively large, the ET is mediated by the chromophore. These calculations do not suggest efficient pathways for electron to hop from Tyr203 to anything other than the chromophore.

TABLE S9: T_{DA} from the chromophore to potential electron acceptors in EYFP using the *Pathways* model

Acceptor	T_{DA} (EYFP)	T_{DA} (EYFP+Cl$^-$)	Ratio (Cl$^-$/no Cl$^-$)	Ratio (EYFP/EGFP)
Tyr203	2.3×10^{-2}	2.4×10^{-2}	1.0	
Tyr145	1.9×10^{-2}	2.7×10^{-2}	1.4	1.1
Tyr92	4.8×10^{-4}	7.1×10^{-3}	14.8	0.3
Tyr143	6.8×10^{-5}	8.5×10^{-5}	1.3	1.1
Tyr151	6.0×10^{-4}	3.3×10^{-4}	0.6	0.8
Tyr200	1.3×10^{-4}	7.6×10^{-5}	0.6	0.9
Tyr182	1.6×10^{-4}	1.6×10^{-4}	1.0	0.3
Phe46	1.4×10^{-3}	1.1×10^{-3}	0.8	1.2
Phe64	7.8×10^{-2}	7.8×10^{-2}	1.0	1.0
Phe71	7.8×10^{-4}	7.8×10^{-4}	1.0	1.0
Phe84	2.3×10^{-4}	2.6×10^{-4}	1.1	0.9
Phe165	1.5×10^{-2}	1.4×10^{-2}	0.9	1.4
Phe223	4.4×10^{-3}	2.9×10^{-4}	0.1	3.4
Trp57	1.3×10^{-4}	2.1×10^{-4}	1.6	0.8

TABLE S10: T_{DA} from Tyr203 to potential electron acceptors in EYFP using the *Pathways* model.

Acceptor	T_{DA} (EYFP)	T_{DA} (EYFP+Cl$^-$)	Ratio (Cl$^-$/no Cl$^-$)
Tyr145	3.1×10^{-4}	2.4×10^{-4}	0.8
Tyr92	5.7×10^{-5}	3.8×10^{-3}	66.7
Tyr143	1.2×10^{-5}	1.1×10^{-5}	0.9
Tyr151	7.7×10^{-4}	8.3×10^{-4}	1.1
Tyr200	3.6×10^{-3}	3.6×10^{-3}	1.0
Tyr182	1.1×10^{-5}	2.2×10^{-6}	0.2
Trp57	6.3×10^{-7}	1.1×10^{-6}	1.7

D. Docking analysis

To evaluate the feasibility of the direct tunneling (from the chromophore to an outside oxidant) and whether ET to a particular residue can lead to an efficient ET to an outside oxidant molecule, we performed docking calculations (see Section III C). The distance between docked species (BQ) and different residues characterizes the accessibility of these residues to an outside oxidant. The resulting structures can be used to calculate tunneling probabilities using the *Pathways* model and to compute electronic couplings using CDFT-CI.

Several clusters of structures were identified. Few of the lowest energy structures corresponded to BQ inserted into the barrel (close to the chromophore). For example, in EGFP,

the fraction of such structures is 6/20 ($\sim 30\%$) and this cluster of conformations ranked as 2nd lowest in energy.

Among surface-docked structures, some correspond the relatively large distances between the chromophore and BQ (e.g., a commonly occurring motif has BQ docked at the bottom of the barrel; for these structures the distance is about 8 Å).

We focused on the structures with the shortest distance to the chromophore, Tyr145, Tyr203, and Tyr92. The structures that have the shortest Tyr145-BQ distance have also the shortest chromophore-BQ distance. The representative structures are shown in Figs. S16 and S17. As one can see from Fig. S16, docked BQ is partially inserted into the surface of EGFP and EYFP. The fraction of such structures among the manifold of the 20 lowest-energy surface-docked structures is 4/20 ($\sim$20 %) for EGFP and those structures are lowest in energy.

(a)BQ docked to EGFP   (b)BQ docked to EYFP   (c)BQ docked to EYFP+Cl$^-$
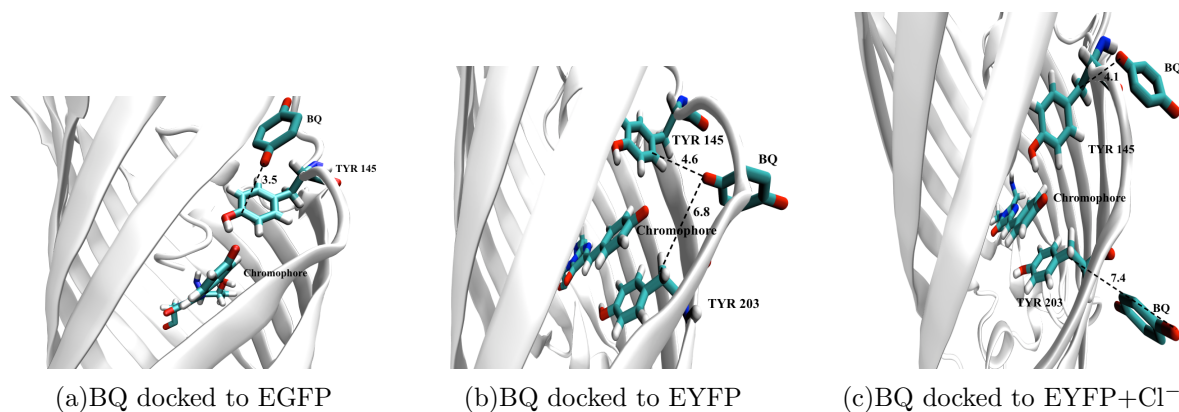
FIG. S16: Benzoquinone docked to EGFP, EYFP, and halide-bound EYFP. In the case of halide-bound EYFP, two docked BQ conformation were obtained, one close to Tyr145 and the other — close to Tyr203. For the structure shown in panel (a), Chro-BQ distance is $\sim$ 6 Å.

As illustrated in Fig. S16, BQ can approach Tyr145 as close as 3.5-4.5 Å (which is similar to the Chro-Tyr145 distance), whereas Tyr203 is considerably less accessible (the shortest computed distance was about 7 Å). Thus, Tyr203 is unlikely to serve as an efficient ET to an outside oxidant; because it is buried inside, it is likely to be a dead end for ET.

To evaluate the possibility of the direct ET mechanism, consider EGFP structure (Fig. S16 a); this structure has the shortest Chro-BQ distance ($\approx$ 6 Å). For this structure, the computed T_{DA} between the chromophore and BQ (docked close to Tyr145) is 4.6×10^{-3}. This value is comparable in magnitude (10 times smaller) to Chro-Tyr145 T_{DA}. Importantly, this pathway for the direct ET is mediated by Tyr145. Thus, Tyr145 is predicted to be important residue for ET both within the hopping and within direct ET mechanisms (more on this in Section IV H).

We performed similar docking analysis for Tyr92; the results are shown in Fig. S17. As one can see, Tyr92 is also unaccessible to outside oxidants (the closest BQ-Tyr92 distance is 8 Å); thus, ET to this residue is unlikely to lead to the redding.

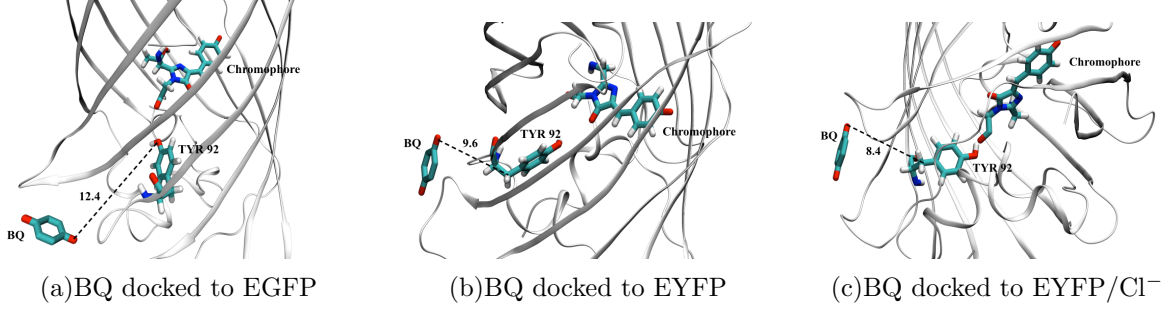(a)BQ docked to EGFP (b)BQ docked to EYFP (c)BQ docked to EYFP/Cl$^-$

FIG. S17: Benzoquinone docked to EGFP, EYFP, and halide-bound EYFP close to Tyr92.

TABLE S11: Electronic couplings for ET involving Chro-Tyr203, Chro-Tyr145, and Chro-mediator-Tyr92 averaged over 41 frames for Chro-Tyr203, Chro-Tyr145, and 19 frames for Chro-Tyr92 on the ground-state surface.

System	QM part	point charges	H_{da}^2(eV^2)		
			Chro-Tyr203	Chro-Tyr145	Chro-Tyr92
EGFP	Chro + Tyr	rest	–	2.14×10^{-1}	3.51×10^{-3}
EYFP (no halide)	Chro + Tyr	rest	1.80×10^{-1}	1.41×10^{-1}	7.60×10^{-4}
EYFP-Y145L	Chro + Tyr	rest	9.70×10^{-2}	–	–
EYFP (with halide)	Chro + Tyr	Cl$^-$ & rest	6.70×10^{-2}	5.90×10^{-1}	4.34×10^{-2}

CDFT-CI with ωB97X-D/cc-pVDZ.
The QM/MM scheme for Tyr92 is shown in Fig. S14.

E. Electronic couplings

The coupling between the chromophore and Tyr145 is very similar to that between the chromophore and Tyr203, both in EGFP and EYFP (no halide). So, in agreement with the *Pathways* model predictions, these two pathways may be competitive. The coupling between the chromophore and Tyr203 is almost 3 times smaller when Cl$^-$ is present. Furthermore, Cl$^-$ affects the ratio of the couplings in EYFP (Chro-Tyr203/Chro-Tyr145): 1.6 in EYFP versus 0.1 in halide-bound EYFP. Thus, in addition to affecting the energetics, chloride binding reduces the coupling between the chromophore and Tyr203, which further slows down the rate. The effect is due to a partial hydrogen bond formation that changes the relative orientation of chromophore and Tyr203. As shown in Fig. S18, in the chloride-bound EYFP, the π-stacking is perturbed leading to reduced delocalization of molecular orbitals. This affects couplings and also explains the observed changes in oxidation energetics (i.e., π-stacking increases ΔG_{ox}, and when π-stacking is perturbed, ΔG_{ox} drops).

The computed couplings between the chromophore and Tyr92 suggest that this ET pathway is not competitive since the coupling is similar in EGFP and EYFP without halide, but EGFP does undergo redding. Also the differential (about $\sim$100 times) coupling values, for chromophore and Tyr92 combination, between EYFP with and without halide results from the change of pathways in these two (Fig. S14). In the presence of halide, the residues slightly change their orientation which leads to a change of the pathways and the difference in coupling values is seen in both the *Pathways* and CDFT-CI calculations.

To investigate the effect of temperature on the couplings, we performed additional calculations for EGFP at T=273 K. As expected, reduced thermal fluctuations lead to the
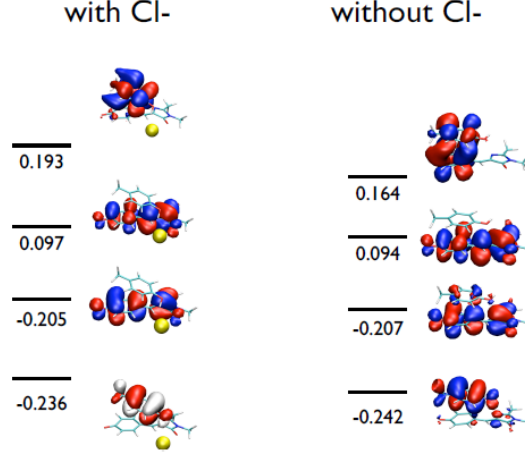
FIG. S18: MOs (energies in hartrees) of the chromophore and Tyr203 in EYFP with (left panel) and without (right) chloride. Note the change of the relative orientation of tyrosine and chromophore and the difference in delocalization.

TABLE S12: Comparison of electronic couplings for ET involving Chro-Tyr203 and Chro-Tyr145 ET averaged over 41 frames in CT state surfaces (H_{da}^2). Electronic couplings were calculated using CDFT-CI with ωB97X-D/cc-pVDZ. Coupling calculations for Chro-Tyr203 and Chro-Tyr145 were performed on the CT203 and CT145 surfaces, respectively.

System	QM part	point charges	H_{da}^2(eV^2)	
			Chro-Tyr203	Chro-Tyr145
EGFP	Chro + Tyr	rest	–	0.011
EYFP	Chro + Tyr	rest	0.040	0.021
EYFP-Y145L	Chro + Tyr	rest	0.014	–
EYFP + Cl$^-$	Chro + Tyr	Cl$^-$ & rest	0.039	0.020

increased electronic couplings for the forward ET, i.e., the computed H_{DA}^2=0.284 eV^2, to be compared with 0.214 eV^2 obtained at 298 K.

F. Gibbs free energies, couplings, and ET rates

Here we summarize the LRA calculations of the free energy and reorganization energy of the ET steps in different proteins. We use the energy differences estimated from extrapolated CDFT-CI values ($\langle \Delta E'_{cdftci} \rangle_g$ and $\langle \Delta E'_{cdftci} \rangle_{CT}$) for the ground- and CT-state surfaces. These energies are summarized in Table S13. Using these energies and the Marcus rate expression, Eq. (4), we compute the ET rate constants for several ET channels, which are collected in Table II of the main manuscript.

For an additional validation of our protocol, we compared our λ with the reorganization for CT from chromophore to Tyr145 in EGFP computed using *Molaris*, a software based on a semi-empirical polarizable model [Ricardo Matute and Arieh Warshel, private communication]. In these calculations, λ was computed using LRA and also using the EVB to obtain the diabatic surfaces and then using Warshel's microscopic version of the Marcus parabolas with a free energy perturbation umbrella sampling (FEP/umbrella sampling)

TABLE S13: Calculated free energies and reorganization energies for overall reaction (Chro$^-$Tyr$\rightarrow$Chro$\cdot$Tyr$^-$) in terms of extrapolated CDFT-CI energy difference, Eqns. (25) and (26). All values are in eV.

System	Final state	$\langle\Delta E'_{cdftci}\rangle_g$	$\langle\Delta E'_{cdftci}\rangle_{CT}$	ΔG_{CT}	λ_{CT}	E_{em}	ΔG^{ex}_{CT}
EGFP	CT 145	3.737	2.046	2.892	0.846	2.44	0.452
EYFP		3.837	2.429	3.133	0.704	2.35	0.783
YFP + Cl$^-$		3.697	2.124	2.911	0.787	2.35	0.561
EYFP	CT 203	3.200	2.627	2.914	0.287	2.35	0.564
EYFP-Y145L		3.380	2.592	2.986	0.394	2.35	0.636
EYFP + Cl$^-$		3.442	2.972	3.207	0.235	2.35	0.857

approach that considers the energy gap as the reaction coordinate. These calculations involved 21 windows of 25 s each and, again, used a polarizable model[32]. The results were: LRA 0.927 eV (0.925 eV contribution from electrostatics) FEP 0.873 eV, to be compared with our value of 0.846 eV. The agreement is very good and also proves that electrostatic embedding is sufficient here. It also validates our scheme for calculating ΔE_{CT}.

Strong coupling limit. We also computed rates in the strong coupling limit, using Eq. (5). The rates are about 3 orders of magnitude lower, but the trend is the same. The r_1 values for EGFP, EYFP, and EYFP+Cl$^-$ are: $2.4 \cdot 10^4$, $3.3 \cdot 10^{-1}$, and $1.1 \cdot 10^3$ s^{-1}, respectively (r_4 in EYFP is $1.3 \cdot 10^2$ s^{-1} and is ≈ 0 in EYFP+Cl$^-$).

G. Kinetic model for ET via hopping mechanism

In this section, we discuss a hopping mechanism for ET. We present relevant energetics and rates and introduce a kinetic model. In section IV H, we discuss an alternative mechanism via direct ET.

Fig. 3 of main text shows our kinetic model of ET via hopping mechanism. Table II (main text) summarizes the computed energetics and relevant rates (at 298 K).

We note that typical $r_f \sim 10^9$ s^{-1}. r_2 is expected to be very fast, as this is an exothermic step. The upper limit is given by the diffusion-limited rate which we estimated as $r_2 = 2 \times 10^{10}$ s^{-1}. If this step is diffusion limited and/or dominated by tunneling, r_2 should be temperature-independent.

We consider the following mechanism for photoinduced ET via hopping. We assume that in EGFP, there is a direct ET pathway from Chro^{-*} to Tyr145, the rate is given by r_1. Once electron reaches Tyr145, it can either go back (r_{-1} and r_3) restoring Chro, or initiate some chemistry (potentially leading to bleaching), or irreversibly tunnel out (r_2, fast), to an outside oxidant forming a red form precursor. There is a competing channel, r_4, to ResX; this channel can lead to either permanent bleaching (r_b) or to restoring the chromophore (r_{-4} and r_5). In EYFP, ResX$\equiv$Tyr203, in EGFP, ResX might be Tyr92 or another acceptor, but it is not as competitive as Tyr203. As illustrated by the *Pathways* and docking calculations, Tyr203 is buried inside the barrel and the pathway for ET from Tyr203 to Tyr145 involves the chromophore thus increasing the probability of quenching. Therefore, r_6 is expected to be slow. As one can see from Table II of the main manuscript, the π-stacking with Tyr203 affects the energetics of ET from the chromophore to Tyr145 suppressing the main channel

for ET (r_1). The anions affect this scheme by modulating the couplings and energetics (ΔG). The analysis reveals that the anions upset π-stacking by changing the orientation of Tyr203 (see section III E 3).

Note that in our calculations, we neglect possible proton transfer that may occur following ET. Proton transfer will stabilize the accepting sites (Tyr145 or ResX) reducing the reverse rates.

By computing the first-passage time[33], the model gives the following expression for the yield of red form precursor:

$$Y_r = \frac{r_1 r_2 (r_{-4} + r_b)}{r_f (r_2 + r_{-1} + r_b)(r_{-4} + r_b) + r_1(r_2 + r_b)(r_{-4} + r_b) + r_4 r_b(r_2 + r_{-1} + r_b)}. \tag{30}$$

The total yield of bleaching is:

$$Y_{totb} = \frac{1}{1 + \frac{r_f(r_2 + r_{-1})}{r_1(r_2 + r_b) + r_4 r_b(r_2 + r_{-1} + r_b)/(r_{-4} + r_b)}}. \tag{31}$$

These bulky expressions can be simplified under the following assumptions: $\frac{r_{-1}}{r_2} \ll 1$ and $\frac{r_{-4}}{r_b} \ll 1$, leading to:

$$Y_r \approx \frac{r_1}{(r_f + r_1 + r_4)(1 + \frac{r_b}{r_2})}, \tag{32}$$

$$Y_{totb} \approx \frac{r_1 + r_4}{\frac{r_f}{(1 + \frac{r_b}{r_2})} + r_1 + r_4}. \tag{33}$$

We can further simplify these expressions by using that r_f is very large relative to other rates. We also note that $\frac{r_b}{r_2}$ term is likely to be small (since r_2 is expected to be much faster than the rate of chemical reactions leading to permanent bleaching) and can be neglected in the present analysis. Under these conditions:

$$Y_r \approx \frac{r_1}{r_f(1 + \frac{r_b}{r_2})} \approx \frac{r_1}{r_f}, \tag{34}$$

$$Y_{totb} \approx (\frac{r_1}{r_f} + \frac{r_4}{r_f})(1 + \frac{r_b}{r_2}) \approx \frac{r_1}{r_f} + \frac{r_4}{r_f}. \tag{35}$$

As expected, the yield of the red-form precursor is predominantly determined by $\frac{r_1}{r_f}$. The yield of total bleaching is approximately equal to the sum of the permanent bleaching via ResX and forming the red-form precursor.

1. Implications of the hopping model

Using Eqns. (34)-(35) and the rates from Table II of the main manuscript, we obtain Y_r(EGFP)=1.5 %, Y_r(EYFP) = 2×10^{-5} %, and Y_r(EYFP+Cl$^-$)=0.2 %. Thus, the hopping model describes the observed differences between the three proteins correctly.

The contributions to the Y_{totb} from the Tyr203 channel are 1.2×10^{-2} % (EYFP), 1.1×10^{-3} % (EYFP-Y145L), and ≈ 0 in the presence of halide. Thus, in the absence of NaCl and the oxidant, the observed EYFP bleaching may be attributed to the ET to the trap site,

Tyr203.

In the strong coupling limit, the computed rates are slower leading to reduced QY, i.e., 0.01 % in EGFP, which is still feasible for redding. Thus, using the Marcus theory in the strong coupling regime leads to the same conclusions.

The effect of mutation of Tyr145 to phenylalanine and leucine is expected to increase ΔG_{CT} by about 0.07 (phenylalanine) or more. This would result in r_1 decrease by a factor of 8-10 in EGFP and EYFP+Cl$^-$, which will reduce the yields proportionally.

For a more quantitative evaluation of the effect of the mutation, we conducted the following calculation. Using a ground-state trajectory for EGFP, we replaced Tyr145 by Phe and computed the energy of the CT state using CDFT-CI energies and the couplings using CDFT-CI/ωB97X-D/cc-pVDZ. We found that ΔE_{CT} does not change (difference of about 0.04 eV), but the coupling drops by a factor of 2.2 (because of the absence of H-bond), which results in about twice slower r_1. This calculation yields an upper bound for the coupling — if one performs a proper equilibrium simulation of the mutant, we expect to observe large structural fluctuations of Phe that will lead to even smaller couplings.

Temperature dependence for hopping model of ET. Within the hopping model, the magnitude of r_1 is determining the yield, see Eq. (34). As one can see from Table II of the main manuscript, this step is endothermic and is expected to slow down at low T. This trend may be partially offset by increased electronic couplings and small increase in fluorescence lifetime. Table S14 shows calculations of rates and yields at different temperatures using the data from Table II of the main manuscript.

TABLE S14: Temperature dependence of the computed rates and yields for EGFP and EYFP+Cl$^-$ assuming T-independent couplings.

T	r_1	Y_r, %	$\frac{r_1}{r_1(298)} = \frac{Y_r}{Y_r(298)}$
EGFP			
310	3.09×10^7	3.1	2.074
298	1.49×10^7	1.5	1.00
288	7.71×10^6	0.8	0.517
278	3.81×10^6	0.4	0.256
273	2.63×10^6	0.3	0.177
EYFP+Cl$^-$			
310	4.52×10^6	0.5	2.342
298	1.93×10^6	0.2	1.00
288	1.30×10^6	0.1	0.674
278	3.97×10^5	<0.1	0.206
273	2.58×10^5	<0.1	0.134

Thus, the hopping model predicts a moderate decline in yields at lower temperature. Electronic couplings slightly increase at lower temperature, which partially offsets this trend. For example, for EGFP at 273 K taking into account the temperature dependence of the couplings yields $Y_r(273)/Y_r(298)=0.23$ (versus 0.18 from Table S14). Additional factor might be slight increase of fluorescence lifetime at low T (but we do not expect it to be large).

To summarize, the hopping model predicts a modest decrease of Y_r at low T, which is in agreement with the experimental observation of a slight decrease of the bleaching yield

at low T. The large increase of the red chromophore formation can be explained by the T-dependence of the slow chemistry step of the red chromophore formation.

H.   ET via direct tunneling

Based on the docking and *Pathways* calculations, we also considered the possibility of the direct ET/tunneling mechanism shown in Fig. 3 (main text).

Docking calculations reveal that the lowest-energy docked structures with the closest BQ-Chro distance correspond to BQ docked closely to Tyr145. The *Pathways* calculations confirm that the direct ET in this structure is mediated by Tyr145. The computed T_{DA} is 4.3×10^{-3} for EGFP when chromophore and BQ is about 6 Å apart, which is 10 times smaller than the Chro-Tyr145 value. Thus, based in this calculation alone, the direct ET is feasible.

To investigate the effect of mutations on ET, we constructed a mutant, EGFP-Y145L, and repeated docking calculations. We found a similar docking site for this mutant. The shortest distance between the docked BQ and the chromophore for EGFP-Y145L is ≈ 6.5 Å (Fig S19).
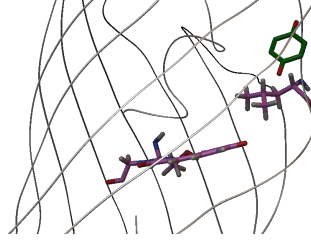

FIG. S19: BQ docked in the vicinity of residue 145 in the EGFP-Y145L mutant.

We then computed tunneling probabilities for the mutant. The results are summarized in Table S15. The probabilities are one order of magnitude smaller than for EGFP. The difference is due to the h-bond between Tyr145 and the chromophore in EGFP (in the *Pathways* model, h-bonds increase tunneling probabilities relative to the through-space pathway, see Section IV C). Thus, docking and *Pathways* calculations predict the decrease of the ET rates via direct ET/tunneling in the Tyr145 mutants.

TABLE S15: Direct tunneling probabilities from the chromophore to the closest docked BQ in EGFP and EGFP-Y145L.

System	T_{DA}	Mediated by
EGFP	4.6×10^{-3}	Tyr145
EGFP-Y145L	3.1×10^{-4}	His148
EGFP-Y145L	1.4×10^{-4}	Leu145

However, the *Pathways* model only captures the effect of DA distance and the connectivity (hydrogen and covalent bonds network) and is not sensitive to the details of electronic structure. To take these effects into account, we computed electronic couplings using CDFT-CI for the two states:

1. $Chro^- - Tyr145/Leu145 - BQ$

2. $Chro^{\cdot} - Tyr145/Leu145 - BQ^-$

In these calculations, Tyr145 acts as a mediating residue. We used a similar protocol as in the CDFT-CI calculations of the Chro-Tyr145 couplings. The QM part in CDFT-CI calculation comprises all three residues; in the ground and CT states, the constraints were applied to the chromophore and BQ, respectively. The rest of the protein was included in the MM part as point charges. We repeated the same calculation for EGFP-Y145L (here the mediator was Leu145).

TABLE S16: Electronic couplings for direct ET from the chromophore to the closest docked BQ in EGFP and EGFP-Y145L.

System	$|H_{DA}|^2, eV^2$
EGFP	2.6×10^{-5}
EGFP-Y145L	2.0×10^{-5}

Surprisingly, the coupling values are much smaller (4-5 orders of magnitude) then the couplings between the chromophore and Tyr145 (0.214 eV^2). Moreover, the difference between EGFP and EGP-Y145L is rather small. Thus, contrary to the *Pathways* calculations, CDFT-CI calculations suggest that (i) couplings are considerably smaller (so the rates might be slower too, although more favorable energetics — exothermic ΔG — may offset and even reverse that); (ii) couplings in EGFP and EGFP-Y145L are very similar. These results strongly argue against the direct ET mechanism.

We did not compute all relevant energetics and ET rates for this mechanism; this would require very extensive calculations. Instead, below we present simple analysis using the data we have. Based on BQ EA, the respective Gibbs free energy change is negative (see Section III E 1). For aqueous BQ, ΔG_{red}=-4.30 eV. When BQ is docked on the protein surface, we expect this value to be less negative (less efficient solvation of BQ$^-$ by the protein surface relative to bulk water). Thus, ΔG for ET from the chromophore to BQ in EGFP is ΔG=-2.189 eV. The maximum rate for ET is achieved when $\lambda = -\Delta G$. Using the computed Chro-BQ couplings (Table S16), the maximal possible ET rate is k_{max}=3×10^{10} s^{-1}. Thus, direct ET might be possible. The rate depends very strongly on λ. For example, using λ=0.85 (largest reorganization energy for Chro-Tyr ET), k=5.8×10^1 (which is too slow for the excited-state ET). In order for the rate to be equal to the rate of Chro→Tyr145 ET, λ should be 1.20 eV. In order to attain the estimated lower-bound of the rate, 10^4 s^{-1}, λ should be 0.96 eV. These are realistic values.

To obtain a more realistic estimate of the rate via direct ET, we computed λ for BQ in aqueous solution using MD and AIMD (B-LYP/6-31+G*) trajectories and ωB97X-D/6-31+G(d,p) for ΔE. λ was computed as a variance (which often[34] overestimates λ relative to so-called Stokes λ that we are calculating in LRA). The resulting values were 1.79 eV (for the AIMD sampling) and 2.74-2.94 eV for the MD sampling. Table S17 lists the rates for direct ET computed using different λ values and the thermodynamic quantities for the chromophores from Table I of the main text and using the following estimates:

$$\Delta G = \Delta G_{ox}(Chro^{-*}) + \Delta G_{red}(BQ) \tag{36}$$

$$\lambda = \lambda_{ox}(Chro^{-*}) + \lambda_{red}(BQ) \tag{37}$$

These expressions assume that the donor and acceptor are sufficiently far and their interaction can be neglected (this is clearly not the case in Chro→Tyr145 calculations). Note that in this approach the lower bound for λ is given by $\lambda_{ox}(Chro^{-*})$.

TABLE S17: Rates for direct ET (Chro^{-*} →BQ) at T=298 K.

System	ΔG, eV	λ, eV	H_{DA}^2, eV^2	k, s^{-1}
λ(BQ)=2.84				
EGFP	-2.189	4.439	2.6E-05	3.2×10^5
EYFP	-1.953	4.240	2.6E-05	1.3×10^5
EYFP+Cl$^-$	-2.376	4.526	2.6E-05	1.0×10^6
EGFP-Y145L	-2.192	4.368	2.0E-05	4.3×10^5
λ(BQ)=1.79				
EGFP	-2.189	3.389	2.6E-05	3.8×10^8
EYFP	-1.953	3.190	2.6E-05	2.3×10^8
EYFP+Cl$^-$	-2.376	3.476	2.6E-05	8.0×10^8
EGFP-Y145L	-2.192	3.318	2.0E-05	4.5×10^8
EGFP	-2.189	1.20	2.6E-05	1.5×10^7
EYFP	-1.953	1.20	2.6E-05	4.1×10^8
EYFP+Cl$^-$	-2.376	1.20	2.6E-05	5.4×10^5
EGFP-Y145L	-2.192	1.20	2.0E-05	1.1×10^7

As one can see, the computed rates contradict the experimental observations. The rates computed from the BQ data are very similar in all four proteins. The rates computed using a smaller value of λ (1.20 eV) show a faster rate in EYFP than in EGFP and a slower rate in EYFP+Cl$^-$. The rate in EGFP-Y145L is almost the same as in EGFP. Thus, these calculations provide a strong argument against the direct ET mechanism.

Using λ=1.20 eV, the anticipated T-dependence for the direct ET is shown in Fig. S20. As one can see, even though this process is exothermic, the Marcus model predicts slower rates at lower T, i.e., r(273)/r(298)=0.5 (again, this trend can be partially offset by the increased couplings and excited-state lifetime).
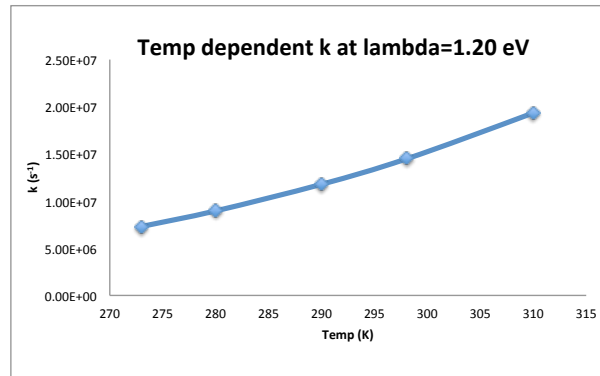

FIG. S20: Rate for the direct Chro-BQ ET using the following parameters: ΔG=-2.189 eV, λ=1.20 eV, $|H_{DA}|^2$=2.6$\times10^{-5}$ eV^2.

One can attempt to estimate the trends in rates using a simpler expression that does not depend on λ and only takes into account trends in ΔG_{ox} from Table I (main text).

As one can see, the redox potentials show the same trend as the ET rates for EGFP and EYFP/EYFP+Cl$^-$ (but not for the mutant). The π-stacking with Tyr203 increases ΔG_{ox} by 0.15 eV, which may slow down the rate by about two orders of magnitude at room T. The chloride decreases ΔG_{ox} thus making the oxidation process feasible.

One can estimate the changes in the rate using these energies and linear free energy approach within a simple one-step model, Chro^{-*} →Chro$^{\cdot}$. In this approach activation energy of a reaction is assumed to be proportional to the change in Gibbs free energy. Rate constant may be then calculated as follows:

$$k \approx exp\big(-\frac{\alpha\Delta G_{ox}}{k_B T}\big) \tag{38}$$

where α is a constant between 0 and 1. Using $\alpha = 0.5$ we calculate relative rate constants for the four proteins:

$$k_{egfp} : k_{yfp} \approx 99 : 1 \tag{39}$$
$$k_{yfp} : k_{yfp+Cl^-} \approx 1 : 3750 \tag{40}$$
$$k_{egfp} : k_{yfp+Cl^-} \approx 1 : 38 \tag{41}$$
$$k_{egfp-Y145L} : k_{egfp} \approx 1.1 : 1 \tag{42}$$

As one can see, the rate of oxidation in EYFP is about 120 times slower than in EGFP; thus, the yield of redding should also drop proportionally. This is consistent with the experiment. However, since the Tyr145→Leu mutation does not affect ΔG_{ox} of the chromophore, the resulting rate in the mutant is almost the same as in EGFP. Thus, these calculations also argue against the direct ET mechanism.

I. Structural analysis

Fig. S21 shows to representative snapshots from EYFP's equilibrium trajectory: the one in which the relative arrangement of the chromophore and Tyr145 is similar to that in EGFP and the second in which Tyr145 moves away from the chromophore and forms a hydrogen bond with His169. The fluctuations in the two distances (Tyr145-Chro and Tyr145-His169) along a 2 ns trajectory are shown in Fig. S22. Fig. S23 shows the distance between the chromophore and Tyr145 along 12 ns equilibrium trajectory. The relative population of the conformation in which the hydrogen bond between Tyr145 and the chromophore is broken (third peak in the histogram) is $\sim$ 37 %.
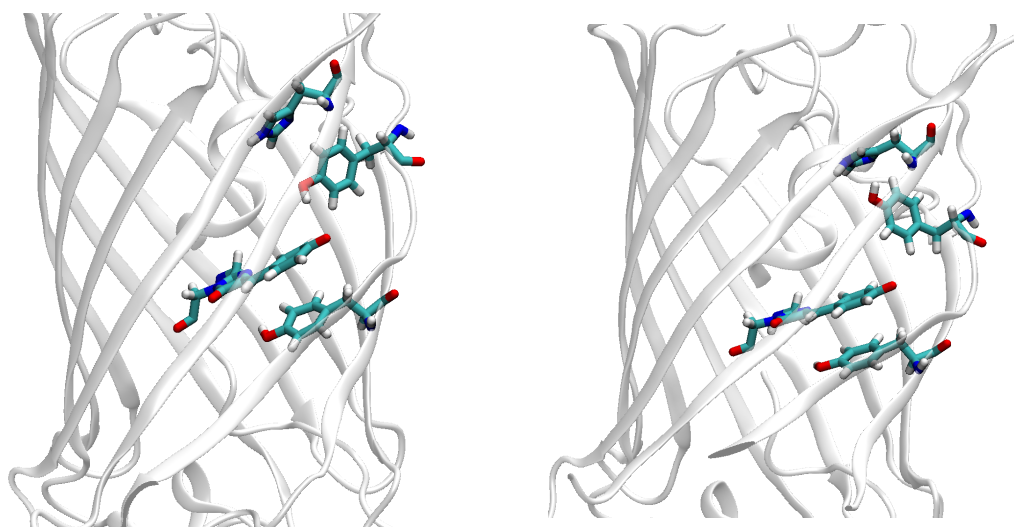
FIG. S21: Two snapshots along the EYFP equilibrium trajectory illustrating two interconverting hydrogen-bond patterns. In the dominant conformation (left), the chromophore forms a hydrogen bond with Tyr145, similarly to EGFP. In the second conformation, Tyr145 flips and forms hydrogen bond with His169.
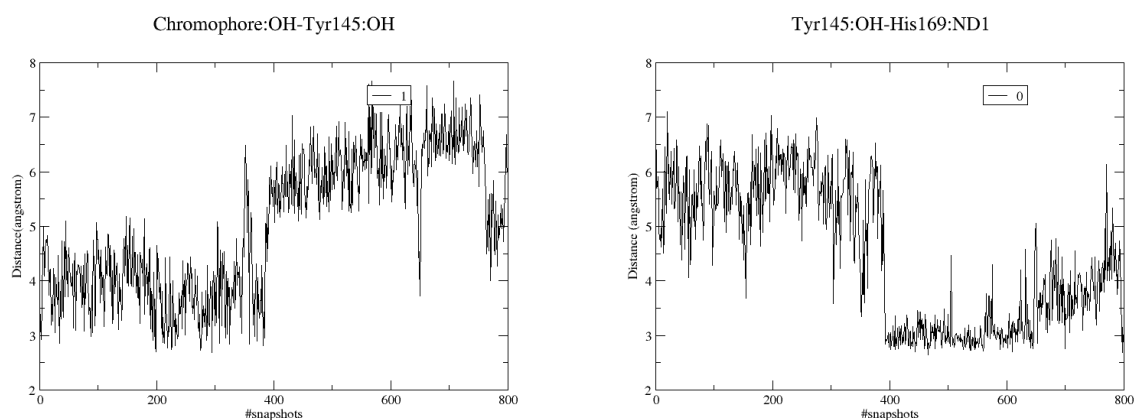

FIG. S22: Distance between the chromophore and Tyr145 (left) and between Tyr145 and His169 (right) along 2 ns trajectory.
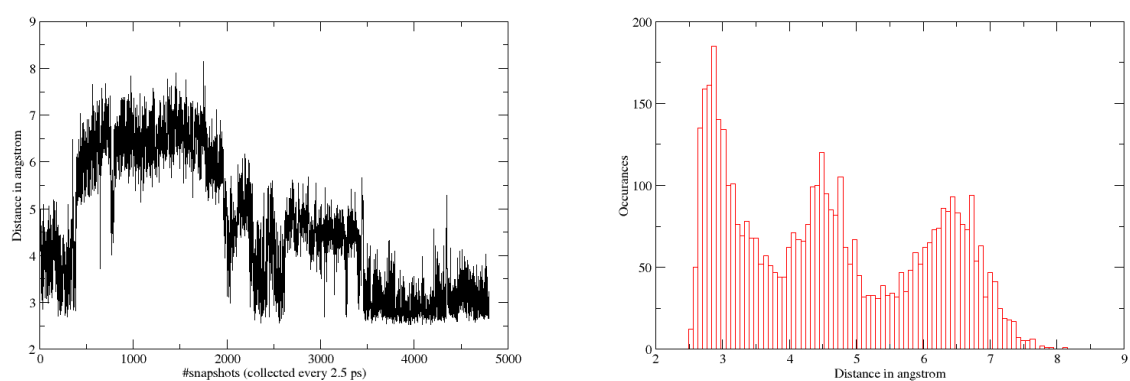
FIG. S23: Left: Distance between the chromophore and Tyr145 along 12 ns trajectory. Right: Chro-Tyr145 distance distribution.

[1] Sinnecker, D.; Voigt, P.; Hellwig, N.; Schaefer, M. *Biochem.* **2005**, *44*, 7085–7094.

[2] Wachter, R.M.; Remington, S.J. *Curr. Biol.* **1999**, *9*, R628–R629.

[3] Bogdanov, A.M.; Mishin, A.S.; Yampolsky, I.V.; Belousov, V.V.; Chudakov, D.M.; Subach, F.V.; Verkhusha, V.V.; Lukyanov, S.; Lukyanov, K.A. *Nat. Chem. Biol.* **2009**, *5*, 459–461.

[4] Jiménez-Banzo, A.; Ragás, X.; Abbruzzetti, S.; Viappiani, C.; Campanini, B.; Flors, C.; Nonell, S. *Photochem. Photobiol. Sci.* **2010**, *9*, 1336–1341.

[5] Jimenez-Banzo, A.; Nonell, S.; Hofkens, J.; Flors, C. *Biophys. J.* **2008**, *94*, 168.

[6] Marcus, R.A. *J. Chem. Phys.* **1956**, *24*, 966.

[7] Marcus, R.A. *Annu. Rev. Phys. Chem.* **1964**, *15*, 155.

[8] Koslowski, T.; Burggraf, F.; Krapf, S.; Steinbrecher, T.; Wittekindt, C. *Biochim. et Biophys. Acta* **2012**, *1817*, 1955–1957.

[9] Sham, Y.Y.; Chu, Z. T.; Tao, H.; Warshel, A. *Proteins: Structure, Function and Genetics* **2000**, *39*, 393.

[10] Olsson, M. H. M.; Hong, G.; Warshel, A. *J. Am. Chem. Soc.* **2003**, *125*, 5025–5039.

[11] Warshel, A.; Parson, W.W. *Q. Rev. Biophys.* **2001**, *34*, 563–679.

[12] Blumberger, J. *Phys. Chem. Chem. Phys.* **2008**, *10*, 5651–5667.

[13] Kowalczyk, T.; Wang, L.-P.; Van Voorhis, T. *J. Phys. Chem. B* **2011**, *115*, 12135–12144.

[14] Balabin, I. A.; Hu, X.; Beratan, D. N. *J. Comput. Chem.* **2012**, *33*, 906–910.

[15] Beratan, D.N.; Betts, J.N.; Onuchic, J.N. *Science* **1991**, *252*, 1285–1288.

[16] Morris, G.M.; Huey, R.; Lindstrom, W.; Sanner, M.F.; Belew, R.K.; Goodsell, D.S.; Olson, A.J. *J. Comput. Chem.* **2009**, *30*, 2785–2791.

[17] NBO 4.0. Glendening, E.D.; Badenhoop, J.K.; Reed, A.E.; Carpenter, J.E.; Weinhold, F. Theoretical Chemistry Institute, University of Wisconsin, Madison, WI, **1996**.

[18] Foloppe, N.; MacKerell, A.D. *J. Comput. Chem.* **2000**, *21*, 86–104.

[19] Reuter, N.; Lin, H.; Thiel, W. *J. Phys. Chem. B* **2002**, *106*, 6310–6321.

[20] Phillips, J. C.; Braun, R.; Wang, W.; Gumbart, J.; Tajkhorshid, E.; Villa, E.; Chipot, C.; Skeel, R.D.; Kale, L.; Schulten, K. *J. Comput. Chem.* **2005**, *26*, 1781–1802.

[21] Wachter, R.M.; Yarbrough, D.; Kallio, K.; Remington, S.J. *J. Mol. Biol.* **2000**, *301*, 157–171.

[22] Ormö, M.; Cubitt, A.B.; Kallio, K.; Gross, L.A.; Tsien, R.Y.; Remington, S.J. *Science* **1996**, *273*, 1392.

[23] Grigorenko, B.L.; Nemukhin, A.V.; Polyakov, I.; Morozov, D.; ; Krylov, A.I. *J. Am. Chem. Soc.* **2013**, *135*, 11541–11549.

[24] Sulpizi, M.; Raugei, S.; VandeVondele, J.; Carloni, P.; Spirk, M. *J. Phys. Chem. B* **2007**, *111*, 3969–3976.

[25] Chai, J.-D.; Head-Gordon, M. *J. Chem. Phys.* **2008**, *128*, 084106.

[26] Chai, J.-D.; Head-Gordon, M. *Phys. Chem. Chem. Phys.* **2008**, *10*, 6615–6620.

[27] Isse, A. A.; Gennaro, A. *J. Phys. Chem. B* **2010**, *114*, 7894.

[28] Wu, Q.; Van Voorhis, T. *J. Phys. Chem. A* **2006**, *110*, 9212–9218.

[29] Wu, Q.; Van Voorhis, T. *J. Chem. Phys.* **2006**, *125*, 164105.

[30] Ding, F.; Wang, H.; Wu, Q.; Van Voorhis, T.; Chen, S.; Konopelski, J.P. *J. Phys. Chem. A* **2010**, *114*, 6039–6046.

[31] Wittekindt, C.; Schwartz, M.; Friedrich, T.; Koslowski, T. *J. Am. Chem. Soc.* **2009**, *131*, 8134–8140.

[32] Warshel, A.; Parson, W.W. *Annu. Rev. Phys. Chem.* **1991**, *42*, 279–309.

[33] van Kampen, N.G. *Stochastic Processes in Physics and Chemistry;* Elsevier, 2 ed., 2001.

[34] Matyushov, D.V. *J. Chem. Phys.* **2013**, *139*, 025102.